Chemical Engineering Journal 451 (2023) 139127

Contents lists available at ScienceDirect

Chemical Engineering Journal

journal homepage: www.elsevier.com/locate/cej

A core–shell 2D-MoS_2@MOF heterostructure for rapid therapy of bacteria-infected wounds by enhanced photocatalysis

Zhenxing Yang [a], Cuihong Chen [a], Bo Li [a], Yufeng Zheng [b], Xiangmei Liu [c], Jie Shen [d], Yu Zhang [e], Shuilin Wu [a,b,*]

[a] Biomedical Materials Engineering Research Center, Collaborative Innovation Center for Advanced Organic Chemical Materials Co-constructed by the Province and Ministry, Hubei Key Laboratory of Polymer Materials, Ministry-of-Education Key Laboratory for the Green Preparation and Application of Functional Materials, School of Materials Science & Engineering, Hubei University, Wuhan 430062, China
[b] School of Materials Science and Engineering, Peking University, Beijing, Yi-He-Yuan Road 5#, 100871, China
[c] School of Health Science & Biomedical Engineering, Hebei University of Technology, Xiping Avenue 5340#, Tianjin 300401, China
[d] Shenzhen Key Laboratory of Spine Surgery, Department of Spine Surgery, Peking University Shenzhen Hospital, Shenzhen, China
[e] Department of Orthopedics, Guangdong Provincial People's Hospital, Guangdong Academy of Medical Sciences, Zhongshan 2nd Road 106#, Guangzhou 510080, China

ARTICLE INFO

Keywords:
Therapy
Photocatalysis
Antibacterial
Wound healing
Molybdenum disulfide

ABSTRACT

As the increasing antibiotics resistance of bacteria, pathogenic bacterial infections aggravate the skin wounds and prevent it from healing and even induce serious complications. Here, we constructed a core–shell interface electric field at the interface between Prussian blue (PB) metal organic framework (MOF) and two-dimensional MoS_2 nanosheets by *in-situ* growth of MoS_2 on the surface of MOF (MoS_2@PBMOF), which drove the transfer of photo-excited electrons and promoted the separation of photoinduced electron-hole pairs. Additionally, the lower O_2 adsorption energy of MoS_2@PBMOF endowed the heterostructure with much stronger O_2 adsorption ability than MoS_2 alone, which provided more oxygen species to capture the photogenerated electrons and holes and thus produced more radical oxygen species (ROS). Meanwhile, the excellent photothermal property of the composite could regulate the release of iron ions from MoS_2@PBMOF under light irradiation by hyperpyrexia. Hence, under 660 nm visible illumination for 20 min, the MoS_2@PBMOF killed 99.73 % *S. aureus* and 99.58 % *E. coli*, which attributed to the synergy of local hyperthermia, abundant ROS, and released iron ions through bacterial membrane damage, protein leakage, and the oxidation of glutathione. Importantly, this composite could promote the healing of damaged tissues with good biosafety by promoting the production of hemoglobin. This work provides new insight into the practical application of promising strategy for environmental disinfection and treating bacterial wound infections without using antibiotics.

1. Introduction

Pathogenic microbial infections including bacteria and virus induced infectious diseases have been threatening the people's health and even life all over the world. For example, the global coronavirus disease 2019 (COVID-19) pandemics has infected more than 450 million people and killed more than 6 million people [1,2]. According to the clinical reports on COVID-19, many patients died from secondary bacterial infections, especially drug-resistant bacteria infections, rather than from the virus itself [3]. It is difficult to treat bacterial infections effectively until the discovery of penicillin by Alexander Fleming in 1928. Since then, antibiotics were extensively used to treat bacterial infections due to their broad-spectrum antibacterial effects [4,5]. Unfortunately, owing to the overuse of antibiotics, a large number of antibiotic-resistant bacteria and even super-bacteria occur [6], conventional drugs have not achieved the desired bactericidal effects [7]. It is urgent to develop antibiotics-free strategies to combat pathogenic bacteria, especially multi-drug resistant (MDR) bacteria.

Some inorganic or organic antibacterial agents are commonly used as effective disinfectants such as silver-based antibacterial agents [8], metal oxides (CuO, ZnO, etc.) [9,10], chitosan [11], and antimicrobial peptides [12], which kill bacteria by releasing metallic ions or disrupting membrane integrity to damage the bacterial membrane. Their shortcomings are long sterilization time required for sufficient

* Corresponding author.
E-mail address: slwu@pku.edu.cn (S. Wu).

https://doi.org/10.1016/j.cej.2022.139127
Received 8 July 2022; Received in revised form 27 August 2022; Accepted 6 September 2022
Available online 8 September 2022

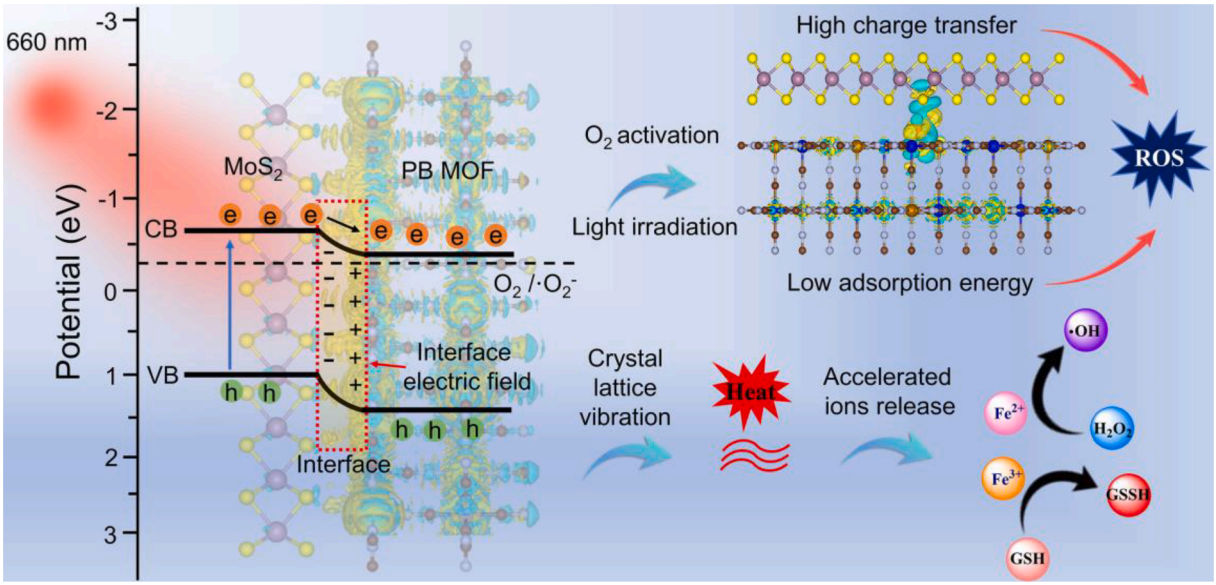

Scheme 1. The schematic illustration of photocatalytic and photothermal effect of MoS_2@PB for effective bacteria-killing under 660 nm irradiation.

bactericidal efficacy and the long-term cytotoxicity and tissue toxicity induced by these antibacterial agents. For instance, on the one hand, the released metals ions such as Ag^+ and Cu^{2+} can accumulate in the main organs and induce lesion [13,14]. On the other hand, some toxic antibacterial ingredients may cause soil and water pollutions during environmental disinfection [15]. Most importantly, the recent studies have shown that bacteria even develop resistance to silver nanoparticles after prolonged contact by genetic variation [16]. In view of these factors, the development of safe, rapid, controllable, and highly effective therapeutic strategies is of great significance and has been attracting more and more attention from scientists and clinicians.

Compared with traditional endogenous antibacterial methods by antibacterial agents themselves, exogenous antibacterial strategies including microwave assisted bactericidal methods [17], ultrasound excited bacteria-killing [18], and light triggered disinfection [19,20], have attracted more and more attention due to the rapid bacteria-killing without inducing bacterial resistance within a short time. Among them, photo-triggered bacteria-killing is portable and low-cost for treating bacterial infected open wounds [21], which generally kills bacteria by photo-triggered hyperthermia locally or photo-produced radical oxygen species (ROS) or the synergistic action of both of them. The deficiency is that highly effective bacteria-killing requires a large amount of ROS or higher temperature of over 60 °C or more locally [22]. However, long time treatment at higher temperatures will destroy healthy tissue and cells [23]. In addition, the yields of ROS produced by photosensitizers are often low because of the following factors. On the one hand, ROS have very short half-life of singlet oxygen (<40 ns) [24], superoxide radicals (1 μs) [25], and hydroxyl radicals (1 ns) [25]. On the other hand, sufficient adsorbed oxygen species and photo-excited electrons and holes are required on the surface of photosensitizers for ROS production. However, most photosensitizers have higher oxygen adsorption energy, which induces low adsorption rate of oxygen species. Furthermore, photo-generated electrons and holes can be recombined easily, which suppressed the photocatalytic performance of photosensitizers. It has been reported that moderate temperature below 55 °C can weaken the bacterial tolerance to ROS by increasing the penetrability of bacterial membrane [26], thus achieving better antibacterial efficiency by the synergy of appropriate quantity of ROS and moderate temperature while ensuring sufficient biosafety [24]. Consequently, there is an urgent need to develop artificial photoresponsive biomedical materials with good photothermal and photocatalytic effects.

Together with its excellent biocompatibility, its two-dimensional (2D) ultrathin atomic layer structure and high specific surface area endow 2D MoS_2 with excellent photo-electrical performances and promising applications in various field, such as optics [27], catalysis [28], electronics [29], and biomedical fields [30]. Although this material can generate ROS through photocatalysis under 660 nm laser irradiation [31,19], the yield of ROS is very low due to its fast electron-hole recombination and poor oxygen species adsorption ability. Therefore, it is necessary to find other suitable functional materials to combine with MoS_2 to improve the photocatalytic performance by suppressing the recombination of photoexcited electron-hole pairs while reducing its oxygen adsorption energy.

Besides possessing the general priority of metal–organic frameworks (MOFs), such as chemical stability, high specific surface area, high porosity, and effective adsorption of oxygen species [32,33], as a kind of MOF, the Prussian blue (PB) has been clinically approved by the US Food and Drug Administration (FDA). Furthermore, this kind of material has low production cost, low biotoxicity, good photothermal performance, excellent biodegradability, and ease of functionalization [34]. Another priority of this material is that the released Fe^{2+} and Fe^{3+} ions from PB can react with hydrogen peroxide (H_2O_2) and Glutathione (GSH) in the inside of bacteria to generate ·OH and consume GSH [35], thereby accelerating the death of bacteria. Additionally, Fe is an important biological element for physiological activities.

In view of the above mentioned, we propose a hypothesis if a composite composed of 2D MoS_2 and PB MOF can be constructed, which has a lower oxygen species adsorption energy, higher separation efficiency of photoinduced electron-hole pairs, thus producing a large amount of ROS and hyperthermia under visible light irradiation. Consequently, this composite can be used for killing bacteria highly effectively through the synergistic action of locally moderate temperature, large amount of ROS and released ferric ions. In this study, a core–shell heterostructure was constructed using PB MOF as a core and 2D MoS_2 nanosheet as a shell (MoS_2@PB). As illustrated in Scheme 1, the introduction of PB in the composite structure successfully enhanced the light absorption capacity of MoS_2 under 660 nm illumination, which further improved the photothermal performance of MoS_2. Meanwhile, formation of MoS_2@PB heterointerface between the two phases increased the separation efficiency of photoinduced carriers and improved the energy evolution pathways and electrons transfer at the interface, thereby significantly enhancing the photocatalytic activity of MoS_2, consequently generating more ROS [36,37]. Moreover, the local hyperthermia caused by the photothermal effect will accelerate the release and penetration of iron

ions into the bacteria, promoting Fenton reaction [35] and oxidation of GSH in bacteria. The advantage of this antibacterial agent is that under 660 nm light irradiation, it can quickly and effectively eradicate bacteria within 20 min without the participation of common and toxic antibacterial heavy metal ions (such as Zn^{2+}, Cu^{2+}, Ag^{+}) and their metal oxides.

2. Experimental section

2.1. Synthesis of PB nanocubes

The PB nanocubes were prepared through a hydrothermal method. Typically, 748.1 mg $K_3[Fe(CN)_6]$ and 9.91 g PVP were dispersed in 132 mL of HCl (0.01 M) under magnetic stirring for 30 min in a 200 mL reactor. Next, the reactor was placed in a constant temperature oven and heated at 80 °C for 22 h. The synthesized materials were centrifuged (10000 rpm, 15 min) and rinsed by using water and absolute ethanol for 3 times. Finally, the prepared PB nanocubes were collected after vacuum drying at 60 °C for 6 h.

2.2. Preparation of MoS_2@PB

83.1 mg PB and 0.814 g Pluronic F127 were added into 72 mL deionized water under ultrasonic. Then 0.835 g molybdate (Na_2MoO_4) and 1.398 g of thiocarbamide (CN_2H_4S) were added into the mixture. The mixed solution was stirred magnetically at room temperature for 30 min, whereafter transferred to a 100 mL autoclave and heated at 190 °C for 9 h. The solution after reaction was separated *via* centrifugation at 11 000 rpm for 10 min. The product was rinsed three times using deionized water and absolute ethanol. The obtained samples then were dried at 60 °C under vacuum for 6 h. As a comparison, the MoS_2 was synthesized the same way as the above method apart from the addition of PB.

2.3. Characterization of materials

The microstructure and morphologies were analyzed through field emission scanning electron microscopy (FE-SEM, ZEISS sigma 500, Germany) and transmission electron microscopy (TEM, Japan, JEM-2100F). The XRD spectra were tested by means of X-ray diffraction (D8 ADVANCE, Bruker, Germany) over a diffraction angle (2θ) range of 5° to 80° in 0.01° steps. The nitrogen adsorption and desorption behaviors were obtained by Brunauer-Emmett-Teller (BET, ASAP 2460). UV–vis spectra were measured by an ultraviolet–visible absorption spectrometer (UV-2600, Shimadzu, Japan). XPS spectra were detected by the (Thermo Scientific 250Xi, USA) instrument. Ion release from the material was performed by using the (ICP-AES, Optimal 8000, Perkin Elmer, USA) instrument. PL spectra tests were conducted by a fluorescence spectrometer (LS-55, PerkinElmer). The zeta potential and hydrodynamic diameter were collected on a Dynamic light scattering (DLS) analysis (Malvern, UK).

2.4. Photothermal performance measurements of materials

The temperature changes of 400 μg/mL of materials (PBS, PB, MoS_2 and MoS_2@PB) were monitored by a thermal imager (FLIR-E50, Estonia) every-one minute under 660 nm visible light irradiation (0.4 W/cm^2, 20 min) and images were captured. Temperature changes of MoS_2@PB were monitored using a thermal imager during three cycles of 20-minute heating and 20-minute cooling. The photothermal conversion efficiency (η) of MoS_2@PB was calculated in accordance with the following equation [23]:

$$\eta = [hS \times (T_{max} - T_0) - Q] / [I \times (1 - 10^{-A})]$$

In the formula, h, S, T_{max}, T_0, Q, I and A denote the heating transfer coefficient, surface area of the heated area, maximum temperature, ambient temperature, heat absorption energy of orifice plate, power of 660 nm laser and absorbance of MoS_2@PB at 660 nm, respectively.

During the cooling process, the time constant (τ_s) are calculated according to the following equation:

$$t = -\tau_s \times \ln\theta = \ln(T - T_0)/(T_{max} - T_0)$$

At this time, assuming that the temperature of the system is very stable, the heat input is equal to the heat output, and the following equation is used:

$$hS = m_s \times C_s / \tau_s$$

In the formula, m_s and C_s are the mass and specific heat capacity of water, respectively.

2.5. Photoelectrochemical measurements of materials

The photoelectrochemical properties of the samples were determined by a three-electrode electrochemical workstation (CHI660E, China), in which the platinum electrode was used as counter electrode, the Ag/AgCl electrode was used as reference electrode, and the sample groups were employed as the working electrode. The photocurrent response and EIS measurements of the samples were carried out with 660 nm visible light as the light source (power 0.4 W/cm^2) and 0.5 M sodium sulfate aqueous solution as the electrolyte. The working electrode was prepared as follows: 4 mg sample powder was dispersed in 1 mL absolute ethanol, and then 150 μL of naphthol solution was added to form a uniform dispersion under ultrasonication. Finally, 50 μL of the above dispersed droplets were placed on the treated titanium sheet with a diameter of 6 mm and dried for 6 h in a 50 ℃ oven to acquire the required working electrode.

2.6. Photodynamic measurements of materials

In order to study $^1O_2$ produced by the samples under 660 nm irradiation, 1,3-diphenyliso-benzofuran (DPBF) was used as an indicator. By calculating the absorption drop at 425 nm [38], the $^1O_2$ produced during photocatalysis was determined. Nitro blue tetrazolium (NBT) dimethyl sulfoxide (DMSO) solution (2.5×10^{-6} mol/L) can react with superoxide radical ($\cdot O_2^-$) to form monoformazan (MF) [39,40]. Therefore, the production of $\cdot O_2^-$ after irradiation can be examined by comparing the absorbance of MF. Hydroxyl radical (·OH) was determined by terephthalic acid (TA) NaOH solution (4 mM) because their reaction product of 2-hydroxyl terephthalic acid (TAOH) had characteristic fluorescence excited by 312 nm at 450 nm [39,40]. The $\cdot O_2^-$ and ·OH of samples were further detected by electron spin resonance (ESR, Bruker EMXplus, Germany) spectroscopy with 5, 5-dimethyl-1-pyrrolin-*N*-oxide (DMPO) as a spin trap under 660 nm red light [41,42].

2.7. Theoretical calculations

We carried out first-principle calculations in the DFT framework using the Vienna AB Initio simulation package (VASP). The exchange correlation energy was described by the Perdew-Burke-Ernzerhof (PBE) form of the generalized Gradient Approximation (GGA) exchange correlation energy functional, in combination with the DFT-D3 correction. The structure optimization of MoS_2 and PB has been performed by changing the positions of all atoms and fixing the lattice parameters until the energy difference of the continuous atomic configuration was$<10^{-4}$ eV. The force per atom in the relaxed structure was$<$0.015 eV/Å. The cutoff energy of the plane wave basis set was set to 400 eV. The k-point spacing on the Brillouin zone (BZ) was set to be$<$0.03 Å^{-1}. The isolated O_2 molecule was put in 10 Å × 10 Å × 10 Å lattices to perform the structure optimizations.

To calculate the adsorption energies of O_2 molecules on PB, MoS_2 surfaces and MoS_2@PB heterojunction, we first constructed the corresponding surfaces. In order to obtain the most stable structures, their structure optimizations were performed by fixing bottom 2 layers and

setting the thickness of 15 Å vacuum. Adsorption energy calculation formula is as follows:

$$\Delta E = E_{system} - E_{slab} - E_{adsorbate}$$

In the formula, E_{system}, E_{slab} and $E_{adsorbate}$ denote the total energies of the adsorption system, substrate surface and adsorbate, respectively.

2.8. In vitro antimicrobial experiments

The antimicrobial ability of materials (PB, MoS_2, MoS_2@PB) was investigated using *S. aureus* and *E. coli* through the spread plate experiment. Firstly, all samples and equipment involved in the experiment were irradiated with an ultraviolet lamp for 30 min in advance for disinfection. Then, 20 μL sterile PBS (control group) or 4 mg/mL of the sample solution (PB, MoS_2, or MoS_2@PB) were aspirated to a 96-well plate containing 180 μL bacterial suspension (1×10^7 CFU/mL). Each sample group was divided into dark and light group. The samples in the dark group were covered with tin foil and placed for 20 min to eliminate the influence of light, while the samples in the light group were exposed to a 660 nm laser (0.4 W/cm^2) for 20 min, but the temperature was maintained at about 55 °C.

After that, the *S. aureus* and *E. coli* suspensions in each well were diluted 100-fold, and 20 μL the diluted bacterial liquid was pipetted and spread equably on the agar plate. The agar plates were placed in a incubator at 37 °C for 1 day, and then the number of colony was counted. Finally, the antimicrobial efficacy was calculated in accordance with the following equation (in which D is the Colony Forming Unit): Antimicrobial efficacy (%) = (D in control group – D in experimental group)/D in control group × 100 %.

In the cycles of bacteria-killing tests, cultured bacteria (1×10^9 CFU/mL) were diluted to 1×10^7 CFU/mL. Then at the end of each antimicrobial test, 200 μL of the bacterial solution was incubated again in fresh medium and used for the next cycle. To evaluate the influence of hyperthermia or ROS alone on the antibacterial performance of MoS_2@PB, the experiments were divided into four groups: Control, MoS_2@PB + Light (19 °C), MoS_2@PB + Water-bath (55 °C), and MoS_2@PB + Light (55 °C). Notably, the temperature of the MoS_2@PB + Water-bath (55 °C) and MoS_2@PB + Light (55 °C) increased for 7 min and kept at 55 °C for 13 min, while the MoS_2@PB + Light (19 °C) group maintained a 19 °C warming and cooling balance in an ice-water bath. The antibacterial experiment of materials under visible light irradiation was performed by 300 W xenon light (0.2 W/cm^2). The method and operational details of the antibacterial experiments are the same as for the 660 nm laser.

2.9. Morphology observation of bacteria

After the antibacterial experiment, the bacterial liquid in the 96-well plate was first abandoned, and then rinsed with sterile PBS for 3 times. Next, 200 μL 2.5 % glutaraldehyde diluent was pipetted to each well, followed by fixation for 2 h. Each well was rinsed for 3 times using sterile PBS, 200 μL ethanol with different concentration gradients (30 %, 50 %, 70 %, 90 %, 100 %) were added and dehydrated for 15 min. Finally, after waiting for the samples to dry, the morphologies of the bacteria were observed with a scanning electron microscope and photographed.

2.10. Live/dead fluorescent staining of bacteria

To visually observe the live/dead states of bacteria, the live/dead fluorescence experiment of bacteria was performed. The samples were mixed with bacteria solution (1×10^7 CFU/mL) and then irradiated with 660 nm visible light for 20 min. The bacterial suspension without the materials was used for the control group. After the antimicrobial operation was completed, the bacteria after different treatments were stained using SYTO9 and PI (Baclight bacterial viability kit, Invitrogen) for 20 min simultaneously and then rinsed with sterile PBS. The photographs were taken with an inverted fluorescence microscope (Olympus, IFM, IX73).

2.11. Protein leakage in bacteria

Bichinchonic acid (BCA) protein assay was adopted to quantitatively determine protein leakage from bacteria. Briefly, after completion of bactericidal experiment, the 150 μL diluted bacterial liquid was mixed with 150 μL sterile PBS, and centrifuged by 6000 rpm for 6 min. Then 25 μL the supernatant was added to 200 μL BCA reagent, and the relative protein leakage was determined on a microplate reader at $OD_{562\ nm}$.

2.12. Ellman's assay

GSH depletion was evaluated using the Ellman's assay [43,44]. In brief, the samples were mixed with 150 μL of GSH bicarbonate buffer solution (0.8 mM) in a 48-well plate and then cocultured at room temperature for 10 min to achieve the equilibrium of adsorption and desorption. Afterwards, the samples were irradiated with a 660 nm laser for 20 min. Subsequently, the supernatant was added into 100 μL 5,5′-dithio-bis-(2-nitrobenzoic acid) (DTNB) (10 mM) and 450 μL Tris-HCl (pH = 8.0, 50 mM), and shook for 20 min to adequately react. As negative control and positive control, 100 μL of PBS and 30 % H_2O_2 were added into 200 μL of GSH solution (0.8 mM), respectively. Finally, the consumption of GSH was calculated through determining the absorbance values at 410 nm on a microplate reader.

2.13. Permeability determination of bacterial membrane

The *ortho*-nitrophenyl-*β*-galactoside (ONPG) assay was conducted to determine the permeability of the membrane (cytoplasmic panniculus) of *S. aureus* on the surface of the samples [45,26]. After the antibacterial process was completed under 660 nm light irradiation or dark conditions, the samples were treated with an ONPG assay kit. The absorbance of supernatant at 420 nm was measured with a microplate reader.

2.14. Cytocompatibility evaluation in vitro

2.14.1. Cell culture and MTT assay

NIH-3 T3 fibroblast cells (Tongji Hospital, Wuhan) were selected as a model to assess the cytotoxicity of different materials using a MTT test. The NIH-3 T3 cells were cocultured with Dulbecco's Modified Eagle Medium (DMEM) including 10 % fetal calf serum and 1 % penicillin–streptomycin solution at 37 °C in a 5 % CO_2 incubator. Before the assay, all materials and equipment were sterilized with 75 % alcohol and a UV lamp about 30 min. The diluted cells suspensions (1×10^5 cells/mL) and different materials were added into the 96-well plate and cocultured for 1, 3 and 7 days, respectively. After that, the DMEM medium was displaced by 200 μL of prepared MTT solution (0.5 mg/mL) and therewith further cultivated at 37 °C for 4 h. Next, the MTT solution in the plate was removed completely, and 200 μL DMSO solution was aspirated into each well with continuous shaking for 20 min to fully dissolve the crystals. The OD value at 490 nm and 570 nm were measured using a microplate reader. The cell viability of samples was obtained through comparing the OD values of each group.

2.14.2. Cell fluorescence staining

To intuitively observe cell morphology, a cell fluorescence staining assay was performed in this experiment. First, the NIH-3 T3 cells and materials were cocultured for 1 day in a 96-well plate. After removing the supernatant solution, the cells spreading on samples rinsed with sterile PBS for 3 times, and therewith immobilized by 4 % formaldehyde for 15 min. Afterwards, the NIH-3 T3 cells were subsequently stained by FITC (YiSen, Shanghai) for 30 min in darkness and rinsed with PBS several times. After that, DAPI (YeaShen, Shanghai) was used to stain the cells for 30 s and then rinsed again with PBS. Finally, the cell morphology on the surface of the samples were observed by an inverted

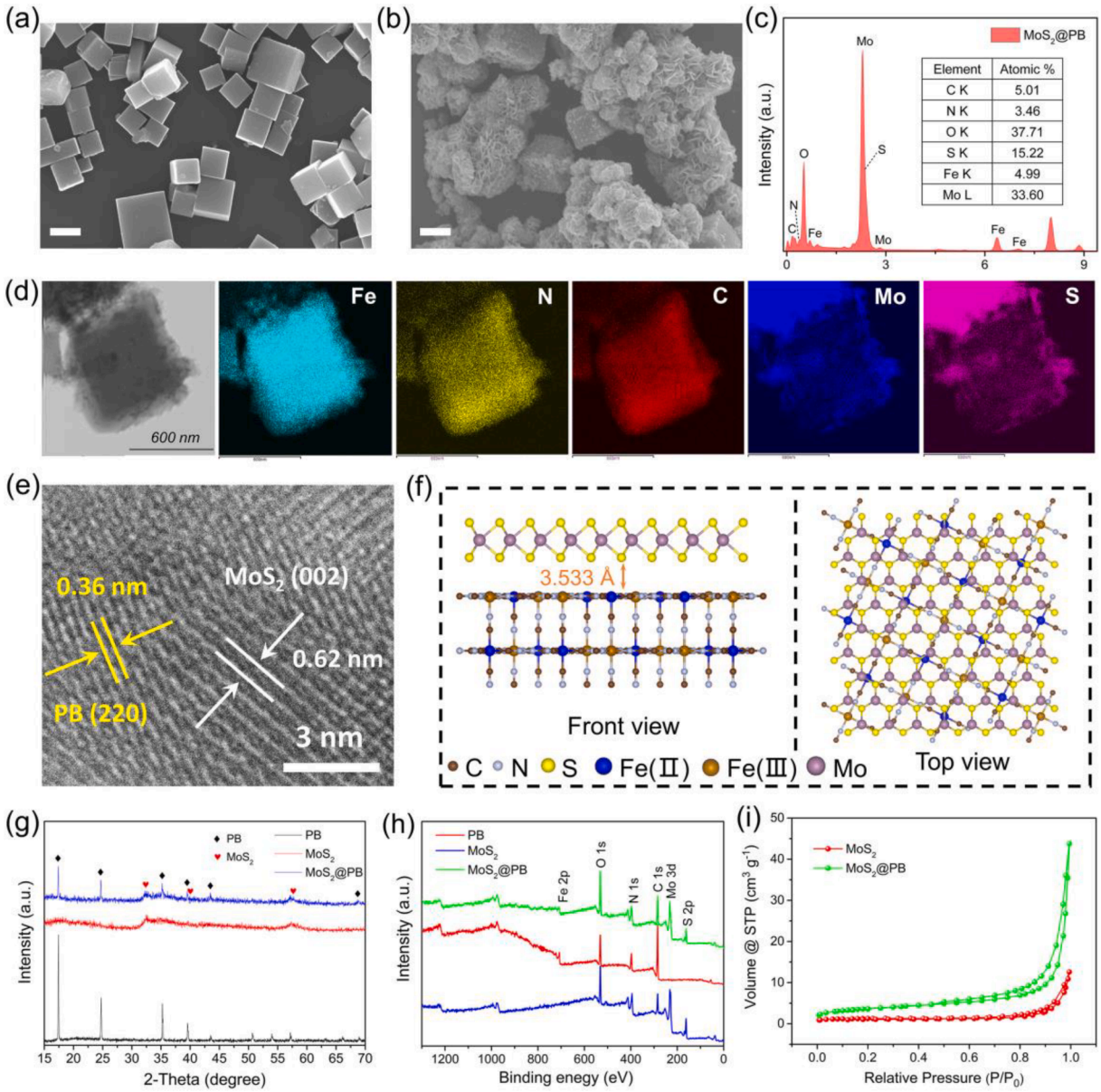

Fig. 1. FE-SEM of (a) PB MOF and (b) MoS_2@PB (scale bars = 500 nm). (c) TEM-EDX of MoS_2@PB. (d) TEM images and corresponding EDX mapping of MoS_2@PB. (e) HRTEM of MoS_2@PB. (f) Crystal structure of MoS_2@PB of different perspectives after structure optimization. (g) XRD of PB, MoS_2 and MoS_2@PB. (h) The XPS survey spectrum of PB, MoS_2 and MoS_2@PB. (i) The nitrogen adsorption and desorption of PB and MoS_2@PB.

fluorescence microscope.

2.15. Hemolytic test

Hemolysis tests of the materials were performed with fresh mouse's blood. The fresh blood was centrifuged (3000 rpm/min, 15 min) and then the serum was removed to collect red blood cells. The red blood cells were rinsed with normal saline three times. Subsequently, 500 μL of a saline solution of materials (800 ppm) were added in 500 μL of a 10 % red blood cell dispersion, respectively. As control, 500 μL of deionized water or normal saline and 500 μL of 10 % red blood cell dispersion were uniformly mixed in a centrifuge tube as a positive control and a negative control, respectively. The mixture was then incubated at 37 ℃ for 4 h. After centrifugation (3000 rpm/min, 15 min) at 4 °C, 100 μL of supernatant solution was aspirated into a 96-well plate, and the absorbance at 570 nm was tested with a microplate reader. The material hemolytic rates (RHR%) were calculated as follows: RHR (%) = (A_{sample} − $A_{negative}$)/($A_{positive}$ − $A_{negative}$). A is the absorbance at 570 nm of the supernatant.

2.16. In vivo antimicrobial experiments

All experimental protocols were agreed by Prevention and the Animal Experiment Center of Huazhong Agricultural University and the Hubei Provincial Center for Disease Control. The test procedure was carried out in accordance with the "Guidelines for the Care and Use of Laboratory Animals in China" and "Regulations on Animal Management of the Ministry of Health of the People's Republic of China". Balb/c male mice (6–8 weeks old, ~25 g in body weight) were obtained from the animal test center of Huazhong Agricultural University. The mice were randomly assigned to one of three groups: Control, 3 M and MoS_2@PB groups. Because of the rapid sterilization, the wound was treated only once, and the wound was treated as follows. Before surgery, 10 % chloral hydrate (30 mg/kg) was injected intraperitoneally into each mouse for anesthesia. The mice were first shaved, then the backs of the mice were then slashed and a biopsy punch was used to create two symmetrical

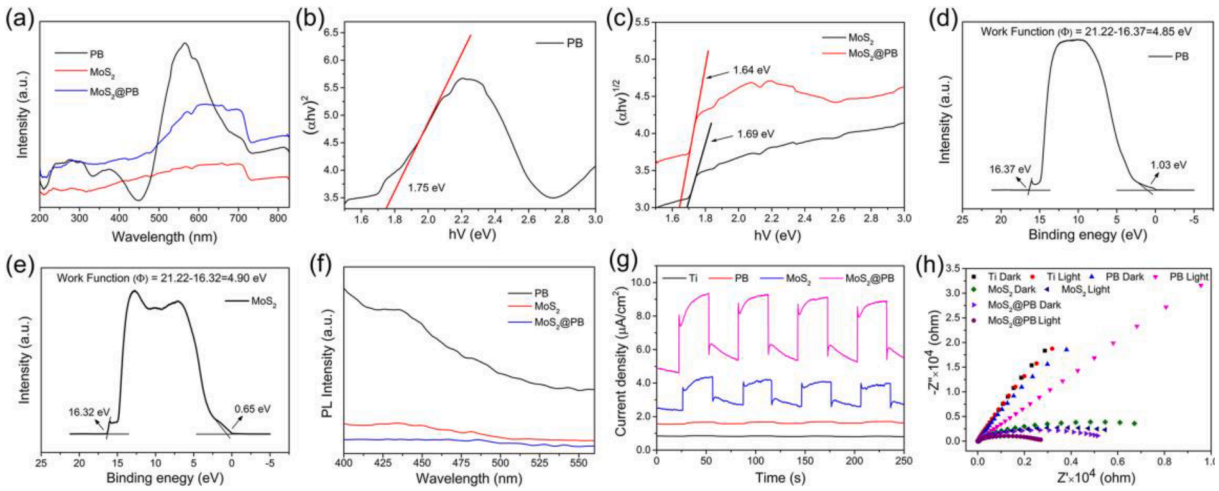

Fig. 2. (a) UV–vis absorption spectra of different groups. (b) Band gap of PB. (c) Band gap of MoS_2 and MoS_2@PB. UPS spectra of (d) PB, and (e) MoS_2. (f) PL spectra of PB, MoS_2, and MoS_2@PB by 325 nm excitation wavelength. (g) Photocurrent response under 660 nm laser irradiation. (h) EIS spectra.

circular wounds of 8 mm in diameter on the left and right sides of each mouse's spine. Subsequently, the wounds of each group were infected with *S. aureus* (1×10^8 CFU/mL, 10 μL) to build an infection model. For the control and 3 M groups, the wounds were disposed of by a 10 μL sterile PBS. Comparatively, in the material group, the wounds were disposed of by using 10 μL MoS_2@PB (0.8 mg/mL). After being irradiated with 660 nm laser for 20 min, the wounds of control and MoS_2@PB groups were covered using hospital gauze. The treated wounds in the 3 M group were bandaged using standard 3 M wound dressings. Then, the mice were raised singly in cages at standard temperature.

Giemsa staining and H&E staining were used to observe wound healing. After 2, 5, 8, 12, and 14 days, photographs of wounds in mice were taken, respectively. Giemsa staining and H&E staining of tissue from the wounds were performed to observe the number of bacteria, inflammation cells, and wound healing process around the wound. Finally, main organs (heart, liver, spleen, lung, and kidney) were collected on day 14 and H&E staining was photographed to assess the *in vivo* biotoxicity of different samples.

2.17. Statistical analysis

All experimental data were expressed as mean ± standard deviation (SD) with $n \geq 3$. Statistical significance was estimated using an unpaired *t*-test. The *p*-value was analyzed using one-way or two-way analysis of variance (ANOVA) and specified in the figure legends.

3. Results and discussion

3.1. Characterization of MoS_2, PB and MoS_2@PB

The morphologies of prepared materials (MoS_2, PB, MoS_2@PB) were exhibited in Fig. 1a, 1b, and S1, respectively. Field-emission scanning electron microscopy clearly exhibited that PB MOF was a regular nanocube and MoS_2 was a nanosphere interwoven with two-dimensional nanosheets. What was more, it could be clearly observed from the morphologies of synthesized MoS_2@PB composite that regular two-dimensional MoS_2 nanosheets have grown *in situ* on the surface of PB. The scale bar measurement showed that the average size of single PB and MoS_2@PB was about 300 nm and 650 nm, respectively, which were well in line with the measurement results of the DLS (Fig. S2). DLS exhibited that the average particle sizes of PB and MoS_2@PB composite in PBS were about 283.0 nm and 692.4 nm, respectively. Meanwhile, the TEM image in Fig. 1d and S3 showed that MoS_2@PB had a typical core–shell heterostructure, with PB as the inner core and MoS_2 nanosheets as the outer shell.

Energy-dispersive X-ray spectroscopy (EDS) (Fig. 1c) demonstrated that MoS_2@PB contained all elements of PB and MoS_2 (Figs. S4 and S5), indicating coexistence of the two materials. According to the EDX mapping (Fig. 1d), Fe, N, and C elements were located at the nucleus, while Mo and S were mainly distributed in the outer shell, indicating 2D MoS_2 nanosheets were homogeneously distributed on the surface of PB. Furthermore, the core–shell heterointerface of MoS_2@PB could be clearly observed in Fig. 1e and S6 through high-resolution transmission electron microscopy (HRTEM), where the lattice fringe spacing of 0.62 nm and 0.27 nm belonged to the typical (0 0 2) and (1 0 0) planes of MoS_2 [32], while the lattice fringe spacing of 0.36 nm and 0.50 nm belonged to the typical (2 2 0) and (2 0 0) planes of PB phase [35]. Fig. 1f showed the atomic structure of the MoS_2@PB heterojunction. According to the density functional theory (DFT) calculation, a stabilized crystal structure was formed and corresponding interface space between PB and MoS_2 was about 3.533 Å, indicating that they are tightly bound.

As shown in Fig. 1g, XRD spectra showed the diffraction peaks at 32.6°, 39.9°, and 57.3°, corresponding to the (1 0 0), (1 0 3), and (1 1 0) crystal face of MoS_2 [46,28], which were also present in MoS_2@PB (marked as MoS_2 with red hearts), indicating that the combination with PB did not change the crystallographic structures of MoS_2. Additionally, the typical crystal face of 17.6° (2 0 0), 24.9° (2 2 0), 35.4° (4 0 0), 39.7° (4 2 0), 43.7° (4 2 2), and 69.2° (6 4 2) of the PB phase also existed in MoS_2@PB (black diamonds marked as PB) [22], indicating the successful modification of MoS_2 onto PB surfaces. Moreover, in Fig. S7, the zeta potential value of PB, MoS_2, and MoS_2@PB were −20.0, −33.7, and −25.2 mV, respectively, and the potential of MoS_2@PB was between PB and MoS_2, indicating that MoS_2 changes its surface charge after growing on the surface of PB MOFs.

X-ray photoelectron spectroscopy (XPS) spectrum (Fig. 1h) showed PB contained four elements C, N, O, and Fe. After MoS_2 nanosheets grew on it, strong signals of Mo and S appeared together with C, N, O, and Fe in spectrum. The Fe 2p high-resolution XPS spectrum of MoS_2@PB (Fig. S8a) had two main peaks at 708.9 and 721.8 eV, belonging to Fe $2p_{1/2}$ and Fe $2p_{3/2}$ of Fe^{3+}, respectively, and satellite peaks at 712.8 and 725.9 eV corresponding to Fe^{2+}, indicating that Fe in MoS_2@PB exhibited a hybrid valence state [22]. The main peaks of C 1 s and N 1 s were at 284.9 eV and 398.1 eV, respectively, which could prove the existence of C—N($[Fe(CN)_6]^{4-}$) in the materials (Fig. S8b and S8c). As shown in Fig. S8d, the binding energies of 232.6 eV and 228.9 eV were attributed to Mo $3d_{3/2}$ and Mo $3d_{5/2}$ of Mo^{4+} [47,48]. Besides, the S 2p spectra of S $2p_{1/2}$ and S $2p_{3/2}$ identified at 161.7 eV and 163.1 eV (Fig. S8e), respectively, which proved the existence of MoS_2 in the

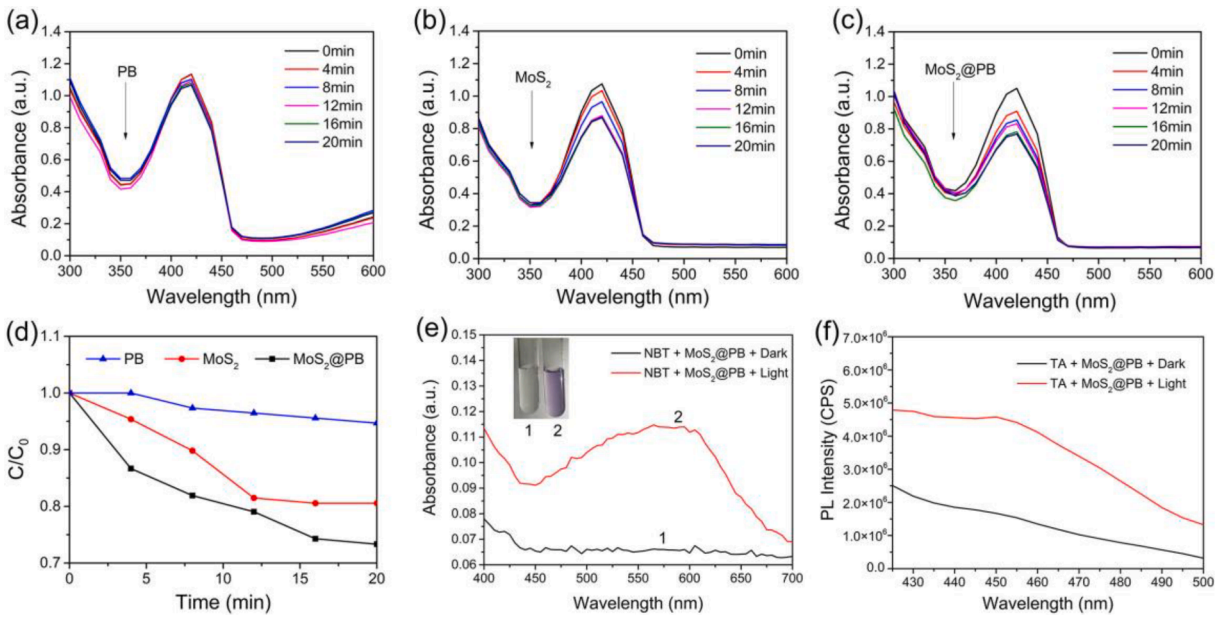

Fig. 3. The $^1O_2$ detected by DPBF degradation of (a) PB, (b) MoS_2, and (c) MoS_2@PB under 660 nm laser irradiation. (d) Contrast curve between PB, MoS_2, and MoS_2@PB. (e) $\cdot O_2^-$ detection of MoS_2@PB using NBT method. (f) ·OH detection of MoS_2@PB using TA.

MoS_2@PB composite [49]. Fig. S8f showed the O 1 s spectrum. This result further confirms the formation of a core–shell heterostructure with the inner core as PB and the outer shell as MoS_2.

The nitrogen adsorption/desorption experiment was performed to characterize the BET surface area of the material. On the basis of Fig. 1i, the BET surface area of MoS_2 increased from 4.067 m^2/g to 12.862 m^2/g after combining with PB MOFs, demonstrating that the introduction of PB improved the BET surface area of MoS_2. PB MOF had a specific surface area of 297.817 m^2/g in Fig. S9.

The above characterization studies confirm that MoS_2 is uniformly dispersed on PB from multiple perspectives, forming a structurally stable MoS_2@PB nanocomposite.

3.2. Photoelectrochemical test and band structure

The optical performance of the material was determined on a UV–vis diffuse reflectance spectroscopy, and Fig. 2a compared the UV–visible absorption among samples. The red curve in the figure showed that the absorption of MoS_2 was primarily in the visible range, but the absorption was weak. The black and blue curves represented PB and MoS_2@PB, respectively. Compared with MoS_2, the introduction of PB dramatically improved the absorption of MoS_2@PB in the visible range due to the strong absorption of PB, especially at the range of 500–720 nm. Hence, MoS_2@PB had a larger light absorption capacity than MoS_2.

To evaluate the production and transfer of photogenerated charges, the bandgap energy of the samples was calculated as follows. In accordance with the plot of the Kubelka-Munk function *versus* bandgap energy, the energy gap of PB, MoS_2, and MoS_2@PB were counted to be 1.75, 1.69, and 1.63 eV (Fig. 2b and 2c), respectively, suggesting that the calculated bandgap of MoS_2@PB was obviously red-shifted compared to MoS_2, which was beneficial to the generation of more photo-excited electrons under 660 nm laser irradiation. Furthermore, the UV photoelectron spectroscopy (UPS) was employed to calculate the band potential of PB and MoS_2 (Fig. 2d and 2e). According to Han et al [50], the corresponding work functions (Φ) of PB and MoS_2 were 4.85 and 4.90 eV, respectively, while the difference between the Φ and the valence band (VB) were 1.03 and 0.65 eV, respectively. Therefore, the VB and conduction band (CB) of PB *versus* NHE were 1.38 and −0.37 eV, respectively, and the VB and CB of MoS_2 *versus* NHE were 1.05 and −0.64 eV, respectively.

The photoluminescence (PL) of the material is mainly because of the recombination of photogenerated carriers. Fluorescence spectroscopy is usually used to probe the migration and recombination process of photogenerated charges in semiconductors, and the decrease in fluorescence intensity means that the probability of carrier recombination decreases. In general, with the decrease of fluorescence intensity, the recombination probability of photogenerated carriers in this sample decreases, which indicated this sample has better photocatalytic performance [51]. The PL spectra in Fig. 2f exhibited that the fluorescence intensity of MoS_2@PB at about 435 nm was lower than that of PB and MoS_2. The weaker fluorescence emission peak suggested the lower electron-hole recombination rate in MoS_2@PB. This result may reflect the rapid transfer of photoinduced electrons from MoS_2 to PB along the heterointerface, hindering the recombination of photoinduced carriers. Therefore, the electron-hole separation efficiency of MoS_2@PB nanocomposites is improved [52].

Additionally, electrochemical impedance spectroscopy (EIS) and transient photocurrent response were used to verify this conclusion. The photocurrent density was measured to evaluate the charge transfer ability of photocatalyst materials. In Fig. 2g, the photocurrents of PB, MoS_2, and MoS_2@PB exhibited good stability and reproducibility in four switching cycles under 660 nm laser irradiation. It was evident that MoS_2@PB had the highest photocurrent density (3.51 $\mu A/cm^2$), which was much larger than other photocurrent density of PB and MoS_2 (1.39 $\mu A/cm^2$), suggesting that MoS_2@PB had a faster charge separation efficiency [53]. Thus, MoS_2@PB exhibited the best photocatalyst property. The EIS tests were performed to determine the impedance of photocatalyst materials. Generally, the smaller semicircle arc in the EIS suggests a smaller electrical resistance [54]. As shown in Fig. 2h, MoS_2@PB had the smallest arc compared to PB and MoS_2, indicating that MoS_2@PB had the highest charge separation efficiency and smallest charge transfer resistance. Moreover, the impedance of the light groups was smaller than that of the dark groups. These results all confirmed that the photocatalytic activity of MoS_2@PB was significantly enhanced after MoS_2 combined with PB, which was beneficial to promote the ROS yield.

3.3. Photocatalytic and photothermal properties

ROS including $^1O_2$, $\cdot O_2^-$, and ·OH is a strong oxidant. It is an active substance generated by the reaction of photogenerated charges with

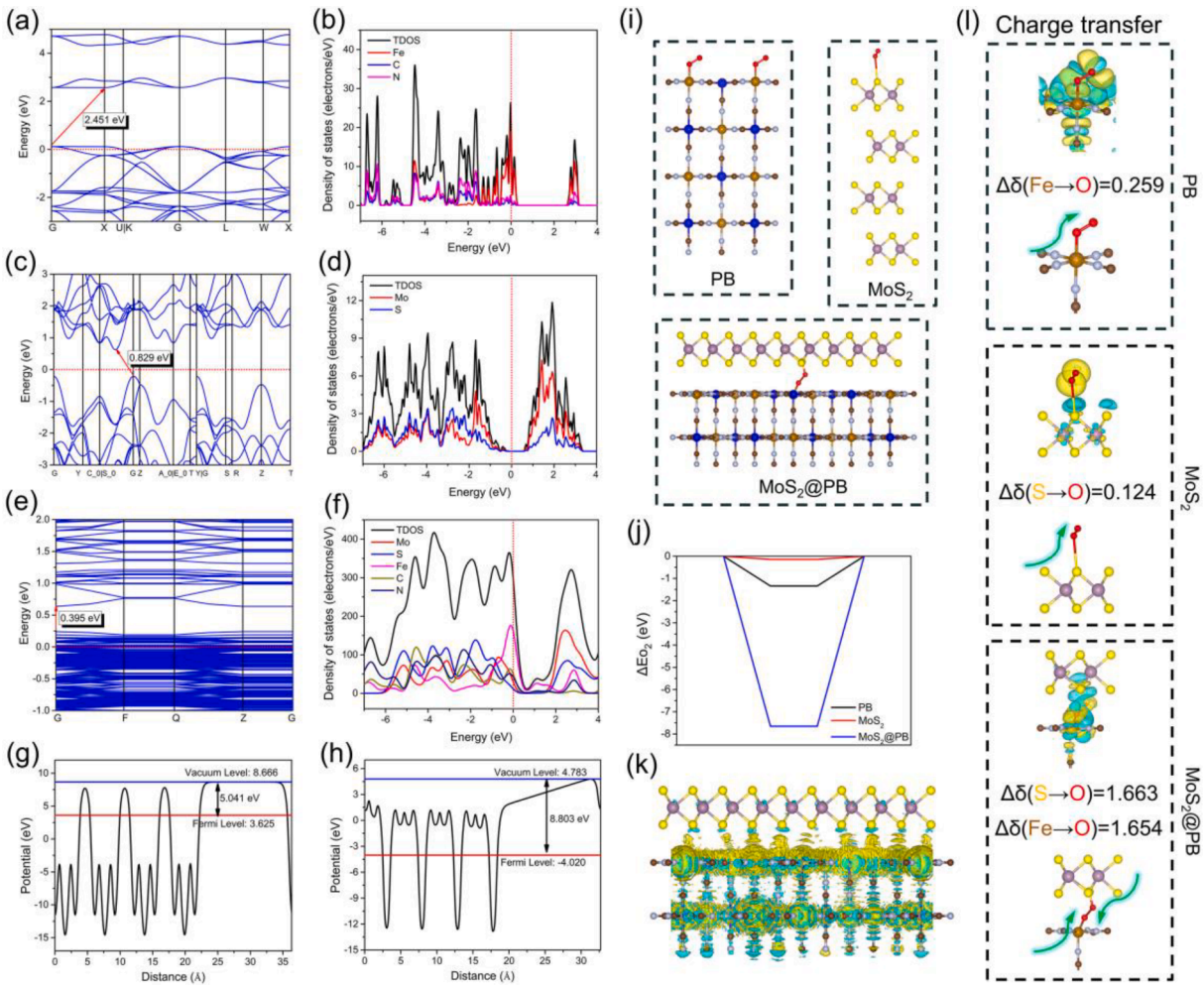

Fig. 4. Electronic band structure and density of states (DOS) of PB (a, b), MoS_2 (c, d) and MoS_2@PB (e, f). The calculated work function of PB (g) and MoS_2 (h). (i) Crystal structures after oxygen absorption on PB, MoS_2, and MoS_2@PB. (j) Adsorption energy of oxygen on the surfaces of PB, MoS_2, and MoS_2@PB. (k) 3D charge density difference of MoS_2@PB. (l) Bader charge calculations of adsorbent O_2.

oxygen or water molecules in the environment [55], which can destroy the oxygen balance inside the bacteria and has a good bacteria-killing ability. The 1,3-diphenylisobenzofuran (DPBF) was utilized to detect the singlet oxygen ($^1O_2$) production of materials by a 660 nm visible illumination. The absorption intensity of DPBF at 420 nm was decreased when specifically reacting with $^1O_2$ [38]. As shown in Fig. 3a, the absorption intensity of the PB group basically unchanged with the extension of the irradiation time, suggesting that PB produce no $^1O_2$ under irradiation. By contrast, the absorption peak intensity of MoS_2@PB group and MoS_2 group at 420 nm decreased gradually, and MoS_2@PB decreased more quickly than MoS_2 (Fig. 3b and 3c), indicating that the introduction of PB greatly improved the photodynamic performance of MoS_2. In addition, the contrast curve further intuitively showed that MoS_2@PB exhibited a higher $^1O_2$ yields than MoS_2 (Fig. 3d).

To further explore ROS types, nitroblue tetrazolium (NBT) and terephthalic acid (TA) were employed to investigate the $\cdot O_2^-$ and ·OH generation of MoS_2@PB, respectively. As shown in Fig. 3e and 3f, compared with the dark conditions, the absorption peak of monoformazan (MF) from 450 to 700 nm and the fluorescence emission peak of 2-hydroxyl terephthalic acid (TAOH) at 450 nm of MoS_2@PB showed characteristic absorption peak after illumination respectively, implying the existence of $\cdot O_2^-$ and ·OH [39,40]. In addition, the $\cdot O_2^-$ and ·OH of samples were further detected using the electron spin resonance (ESR) spectroscopy [41,42], respectively. As shown in Fig. S10, there were obvious signals for $\cdot O_2^-$ and ·OH detected under light illumination, indicating the production of $\cdot O_2^-$ and ·OH [41,42].

To study the photocatalytic mechanism of MoS_2@PB heterostructure, the band structure and density of states of PB, MoS_2, and MoS_2@PB were calculated by the first-principles calculations. The Fermi level was set as 0 eV for reference. Fig. 4a and 4c showed the calculated bandgaps of the PB, MoS_2 were 2.451 and 0.829 eV, respectively. When the monolayer MoS_2 was adsorbed on the surface of PB, the valence band maximum (VBM) of the composite system moved towards the Fermi level obviously, decreasing the band gap to 0.395 eV (Fig. 4e). The calculated energy band showed the same decreasing tendency as the previous experimental results, which may be due to the strong interaction between PB and MoS_2. Simultaneously, compared with PB and MoS_2 (Fig. 4b and 4d), the corresponding DOS results of MoS_2@PB heterostructure displayed more hybridization at the Fermi level, suggesting that electron transfer and interfacial reaction occurred between PB and MoS_2 (Fig. 4f).

To probe the process of interface charge transfer in the MoS_2@PB heterojunction, the calculated work function of the PB and MoS_2 were calculated through DFT calculations [56]. In Fig. 4g and 4 h, the work functions of the PB and MoS_2 were 5.041 eV and 8.803 eV, respectively. This suggested that the Fermi energy level corresponding to MoS_2 was lower than PB. As a result, electrons from the PB surface could transport to the MoS_2 surface through the interface when in close contact with MoS_2 in the dark. Therefore, this confirmed that an interfacial electric field can be established because of the redistribution of charges between

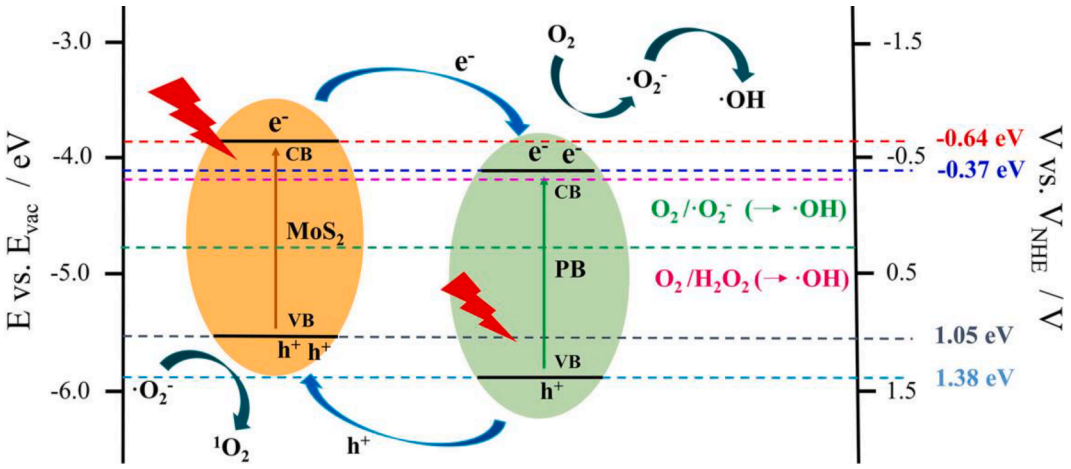

Fig. 5. Photocatalytic mechanism of ROS production after combining PB and MoS_2 under 660 nm irradiation.

two semiconductors in close contact, thus hindering the recombination of photogenerated charge. The details will be further discussed through the subsequent charge density difference and planar-averaged electron density difference.

Moreover, in addition to charge transfer at the heterointerface, the oxygen adsorption state on the material surface was also a significant factor for the generation of $^1O_2$ and $\cdot O_2^-$. The O_2 adsorption energy and the location of O_2 on different material surfaces (PB, MoS_2, and MoS_2@PB) were further investigated by DFT calculations. In Fig. 4i, the O_2 adsorption site of MoS_2 was the S atom while for PB was the Fe (III) atom. For MoS_2@PB, the O_2 binding site at the heterointerface were the S and Fe (III) atoms, respectively. As shown in Fig. 4j, the corresponding order of O_2 adsorption energy was MoS_2@PB < PB < MoS_2, thus demonstrating the optimal O_2 absorption capacity of the MoS_2@PB heterostructure. Additionally, the 3D charge density difference of MoS_2@PB is shown in Fig. 4k, in which the yellow and green areas represent charge accumulation and depletion, respectively. According to the planar-averaged electron density difference, there were approximately 0.000673 e/Å^2 electron transfers from PB to MoS_2 at the heterointerface by calculation (Fig. S11). The outcomes were consistent with Fig. 4g and 4 h. This demonstrated that an interfacial electric field was established between PB and MoS_2, thereby promoting the separation of photoinduced carriers [57].

Besides the adsorption energy of oxygen, the oxygen activation energy is the most important parameter in the catalytic process of materials, and the foreign electrons transferred to the O_2 plays an important role in the oxygen activation [39]. Therefore, the Bader charge calculations and their charge density difference were performed *via* DFT calculations. Specifically, the direction and amount of charge transferred from MoS_2, PB surfaces and MoS_2 heterojunction to O_2 molecule were shown in Fig. 4l, respectively. In the MoS_2 model, there was 0.124 electron charge from S atom to O_2 adatoms through the formed S—O bond, Whereas for PB model was 0.259 electron charge from Fe (III) atom to O_2 adatoms because of Fe—O (adatom) bonding. As for MoS_2@PB, 1.663 and 1.654 electron charge were transferred from S and Fe (III) atoms to adsorbed O adatoms on account of the forming of S—O (adatom) bonding and Fe—O (adatom) bonding, respectively. The results of Bader charge calculations indicated that the MoS_2@PB heterojunction can increase the amount of electron transfer to adsorbed O_2 molecules.

On the basis of the above experimental results, the mechanism of photocatalytic enhancement was given in Fig. 5. The band structure type of MoS_2@PB is a typical type II heterostructure. When exposed to a 660 nm visible illumination, MoS_2 with a narrow bandgap of 1.69 eV could generate ROS. However, due to the severe electron-holes recombination and poor oxygen absorbing ability, a little amount of ROS was generated. When a core–shell heterogeneous interface was formed between the outer MoS_2 and the inner PB, the electron transport speed and separation efficiency of the photoinduced electrons and holes were accelerated, that was beneficial to the generation of ROS. The photocatalytic performance was also significantly improved.

As shown in Fig. 5, when irradiated by 660 nm light irradiation, MoS_2 and PB were excited to produce photoinduced charges in the CB and VB. Because MoS_2 has a more negative CB potential (-0.64 eV vs NHE) than PB (−0.37 eV vs NHE), photoexcited electrons on the MoS_2 surface could be transferred to PB, which facilitated the separation of photoexcited charges from MoS_2. Additionally, since the CB potential of MoS_2 (-0.64 eV vs NHE) is more negative than the standard potential of $O_2/\cdot O_2^-$ (−0.33 eV vs NHE), the photoinduced electrons would react with O_2 molecules to generate $\cdot O_2^-$ [58], then the generated $\cdot O_2^-$ could further react with photoinduced holes to form $^1O_2$. Besides, ·OH was derived from the two-step translation route of $\cdot O_2^-$ in Fig. 5 [58,59]. Therefore, the above results confirmed that MoS_2@PB composites had good photocatalytic activity with a 660 nm laser irradiation.

In Fig. 2a, since the incorporation of PB MOF significantly enhanced the light absorption intensity of MoS_2@PB at 500–720 nm, MoS_2@PB might possess an excellent photothermal performance under 660 nm illumination. Fig. S12a showed the heating curve of the samples with a 660 nm (power density: 0.4 W/cm^2) laser irradiation. After 20 min of light, the temperatures of MoS_2 and PB increased from 26.8 °C to 53.5 °C and 64.5 °C, respectively. In contrast, the temperature of MoS_2@PB increased from 26.8 °C to 57.8 °C under the same condition, suggesting that the combination with PB improved photothermal performance of MoS_2 under 660 nm light irradiation. The corresponding real-time infrared thermal images were shown in Fig. S12c. Beyond that, the repeatable rising/cooling curves shown in Fig. S12b further indicated that the photothermal property of the MoS_2@PB was very stable after three irradiation cycles. The photothermal conversion efficiency (η) of MoS_2@PB also was calculated shown in Fig. S13. Based on the corresponding maximum temperature and time constant (τ_s = 224.54), the photothermal conversion efficiency of MoS_2@PB was 39.30 %, which further demonstrated the high photostability of MoS_2@PB under 660 nm red light illumination.

3.4. Antibacterial study and the mechanism

Two typical pathogens of *Staphylococcus aureus* (*S. aureus*, gram-positive) and *Escherichia coli* (*E. coli*, gram-negative), are commonly used as bacterial models in the bacterial-killing tests [60,61]. Here, they were utilized to study the antimicrobial property of various materials. The antibacterial properties of as-prepared materials *in vitro* were assessed using the spread plate method. As shown in Fig. 6a and 6c,

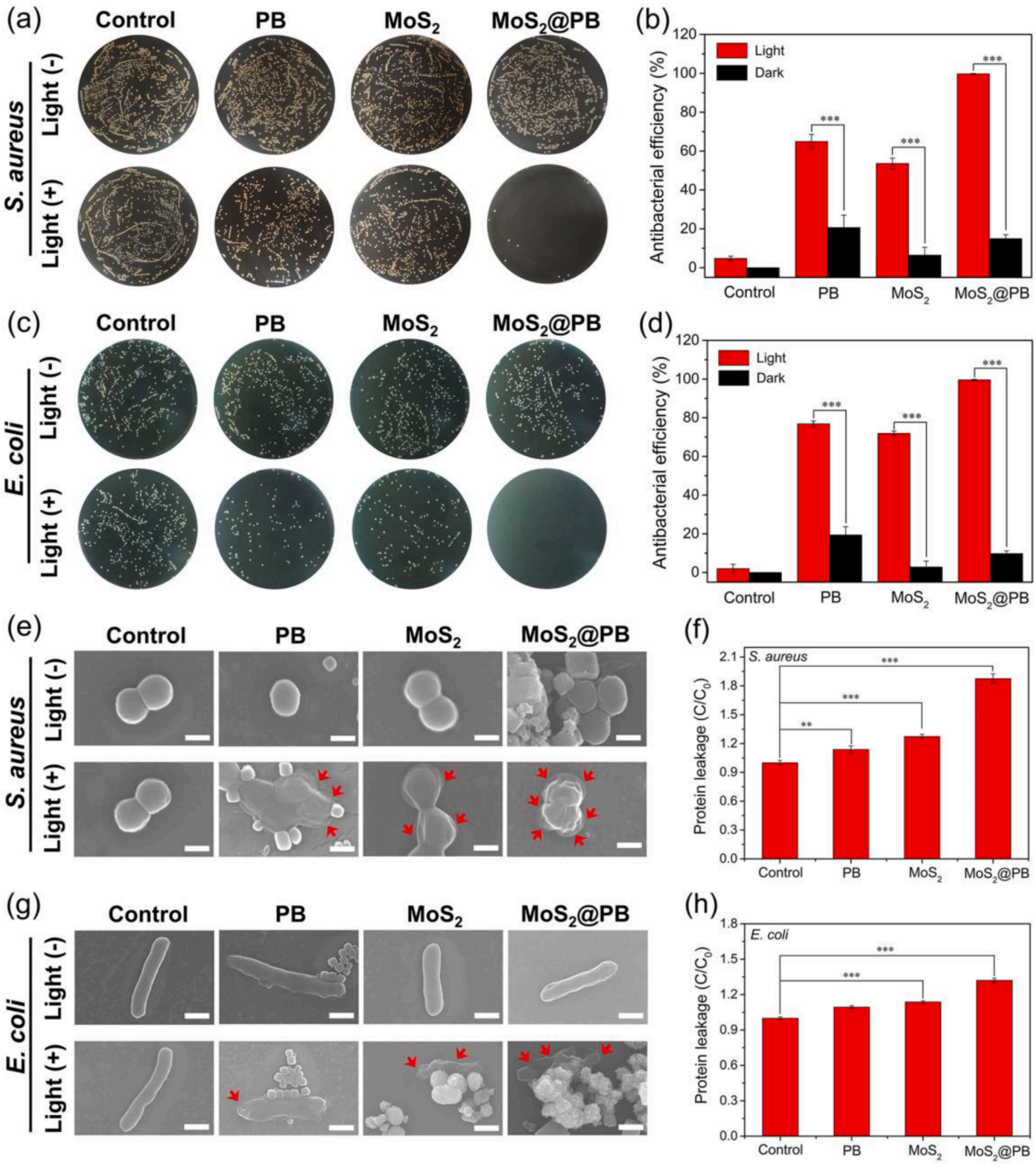

Fig. 6. The results of spread plate test of (a) *S. aureus* and (c) *E. coli* on different samples; The corresponding antimicrobial rates of the samples against (b) *S. aureus* and (d) *E. coli* according to the spread plate pictures; SEM photographs of the morphologies of (e) *S. aureus* (Scar bar = 500 nm) and (g) *E. coli* (Scar bar = 1 μm) from different samples; Protein leakage of (f) *S. aureus* (h) *E. coli* after irradiation. (n = 3, mean ± SD: *$p < 0.05$, **$p < 0.01$, ***$p < 0.001$);

compared with the dark groups, the antibacterial efficacy of the corresponding light groups against *S. aureus* and *E. coli* were significantly enhanced. After 660 nm illumination for 20 min, the antibacterial efficiency of PB, MoS_2, and MoS_2@PB were 64.97 %, 53.63 %, and 99.73 % against *S. aureus* (Fig. 6b) and 76.84 %, 71.93 %, and 99.58 % against *E. coli* (Fig. 6d), respectively. The antibacterial results suggested that the MoS_2@PB group had the most excellent and fastest antibacterial activity under 660 nm light irradiation. Moreover, after three cycles of bacteria-killing tests, the MoS_2@PB displayed circulatory antibacterial ratio over 99 % (Figs. S14b and S14d), and the corresponding spread plate images were shown in Figs. S14a and S14c. From these results, MoS_2@PB exhibited good cycle sterilization performance and reusability. In order to demonstrate the influence of hyperthermia and ROS on antibacterial performance. The antibacterial experiment was carried out by dividing into the following four groups: Control, MoS_2@PB + Light (19 °C), MoS_2@PB + Water-bath (55 °C), and MoS_2@PB + Light (55 °C). The corresponding antibacterial efficiencies of MoS_2@PB + Light (19 °C), MoS_2@PB + Water-bath (55 °C), and MoS_2@PB + Light (55 °C) were 36.84 %, 61.46 %, and 99.63 % shown in Fig. S15 respectively, which suggested hyperthermia alone has a higher bactericidal efficiency than ROS alone, and the antibacterial mode alone cannot achieve complete and effective killing of bacteria. In addition, the antibacterial properties of the materials under visible light irradiation were also evaluated as a comparison under 660 nm light irradiation. Fig. S16 exhibited that the

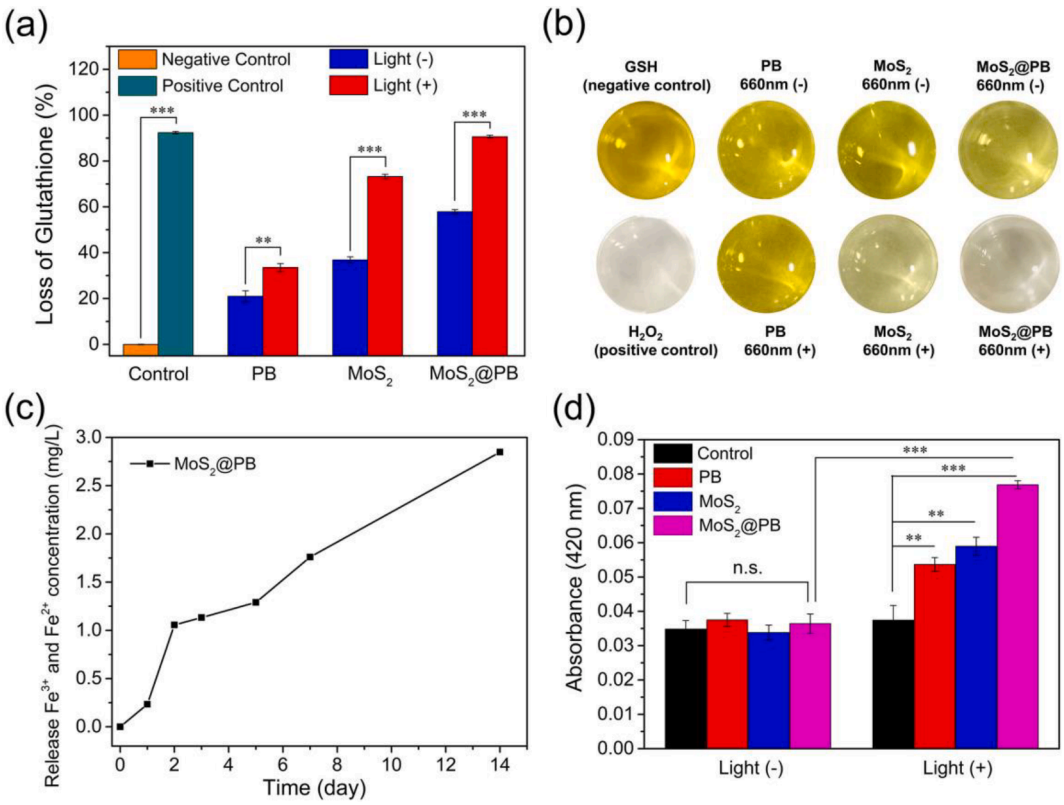

Fig. 7. (a) GSH deletion ability of PB, MoS_2 and MoS_2@PB. (b) Corresponding discoloration photographs of different samples treated with GSH. (c) Cumulative amounts of Fe^{3+} and Fe^{2+} released from the MoS_2@PB. (d) Membrane permeability of bacterial cells evaluated by ONPG hydrolysis assay on PB, MoS_2, and MoS_2@PB. The error bars represent means ± SD, n = 3. ns greater than 0.05, $*p < 0.05$, $**p < 0.01$, $***p < 0.001$.

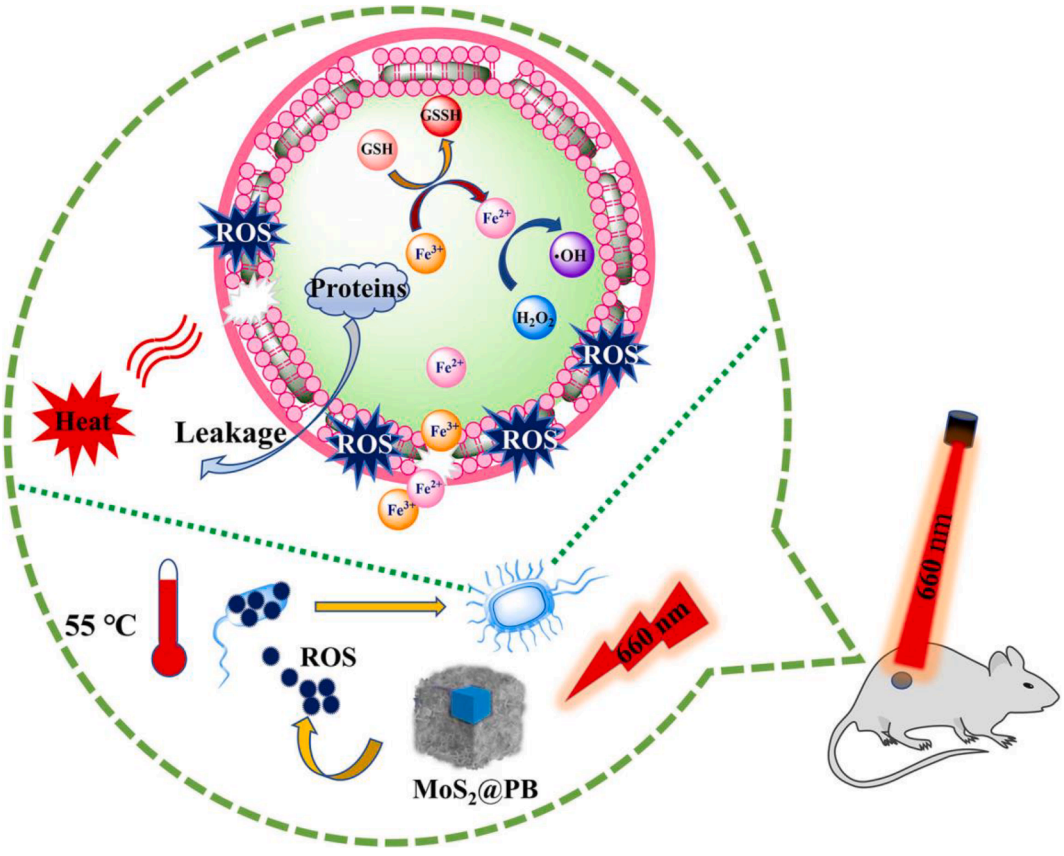

Fig. 8. Bactericidal mechanism of optimized synergistic effect of hyperthermia, ROS and released ions for wound healing.

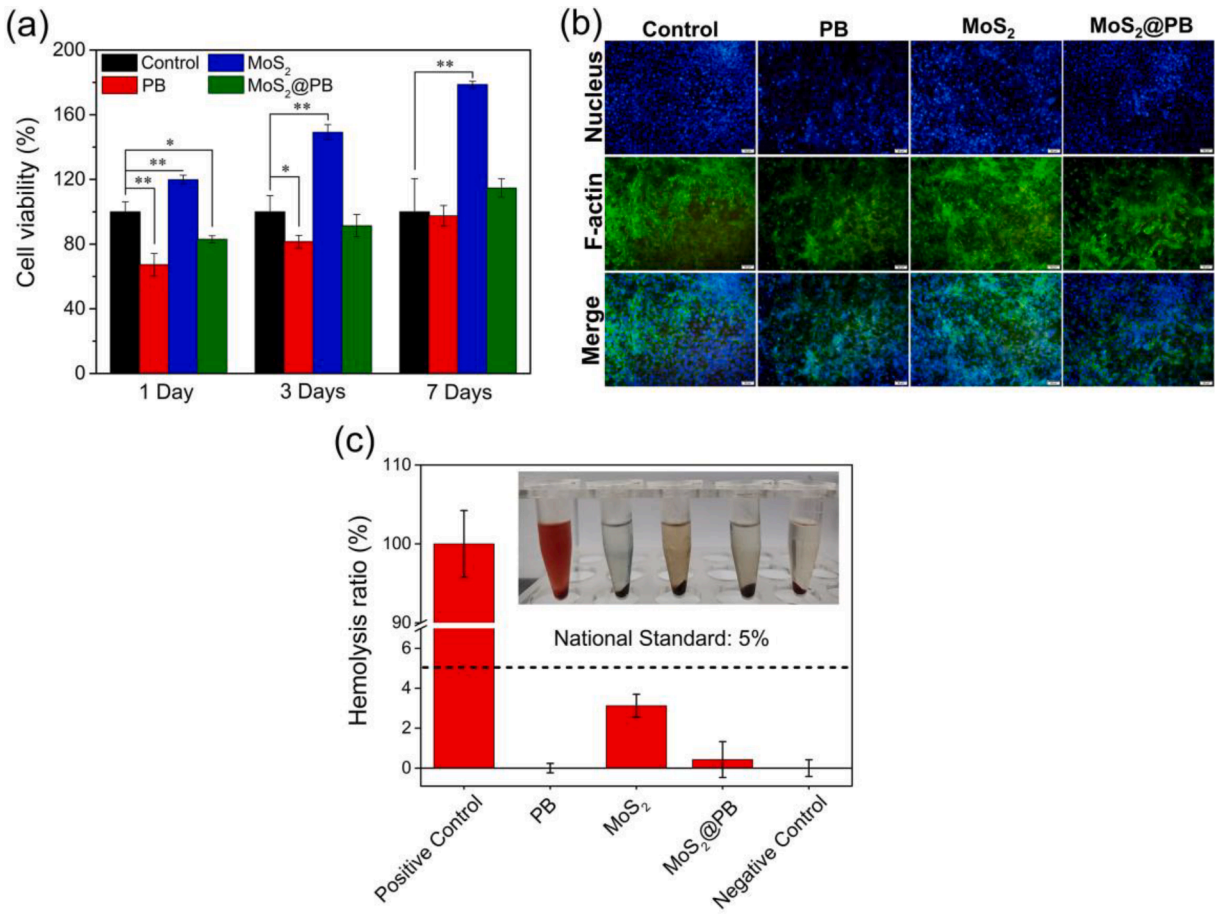

Fig. 9. (a) The viability of NIH-3 T3 cells cocultured with the materials at 1, 3, and 7 days. (n = 3, $*p < 0.05$, $**p < 0.01$, $***p < 0.001$). (b) Fluorescent staining images of cells after 1 day of incubation with different samples (scale bar = 50 μm). (c) Hemolysis rate of different samples.

antibacterial rates of PB, MoS_2 and, MoS_2@PB under light were only 55.75 %, 59.18 %, and 74.02 % against *S. aureus* (Fig. S16b) and 59.08 %, 63.25 %, and 79.41 % against *E. coli* (Fig. S16d), respectively, indicating the lower bactericidal efficiency compared with 660 nm light irradiation.

To further evaluate the antibacterial performance of materials, surface morphologies of different treated *S. aureus* and *E. coli* were observed by FE-SEM (Fig. 6e and 6 g). Under dark conditions, the bacteria of experimental groups or the control group maintained a smooth surface and intact shape, suggesting no obvious damage of bacterial membrane. By comparison, after 660 nm illumination for 20 min, the membranes of bacteria in the PB and MoS_2 groups were significantly wrinkled and damaged. Moreover, the bacterial membranes in the MoS_2@PB group contracted more severely and even ruptured (signaled by red arrows), that attributed to the synergy effect of high temperature and abundant ROS generated by the MoS_2@PB under illumination. Damage to cell membranes is often accompanied by severe protein leakage. As shown in Fig. 6f and 6 h, the MoS_2@PB group with the highest antimicrobial efficiency under light had the most leaked proteins, which was also in line with the antibacterial results and bacterial morphology.

In order to intuitively observe the antibacterial activities, the viability of germs was qualitatively assessed by live/dead fluorescent staining assays, and the corresponding fluorescent images were shown in Fig. S17. The fluorescent images were mostly green under dark conditions, indicating that all materials showed negligible antibacterial properties in darkness. After 20 min of 660 nm laser illumination, partial red fluorescence clearly emerged in PB and MoS_2 groups, whereas almost no green fluorescence appeared in MoS_2@PB group, indicating that MoS_2@PB exhibited efficient antibacterial effect. These above results were well in line with the spread plate results.

Glutathione (GSH), as a thiol-containing tripeptide, is the main endogenous antioxidant in bacteria and can be used as an important indicator of cellular oxidative stress. GSH can be converted to glutathione disulfide (GSSG) under oxidation conditions [43,44]. Ellman's assay was utilized to assess the GSH consumption capacity of materials. Fig. 7a showed the loss of GSH of different materials before and after illumination. After 20 min incubation with the materials in the dark, the loss of GSH in the PB and MoS_2 groups was 20.9 % and 36.8 % respectively. The weak oxidative ability of PB comes from the release of iron ions in PB, and MoS_2 also can facilitate oxidization of organic mercaptans (R–SH) to generate disulfide (R—S—S—R) [62]. As for MoS_2@PB group, the consumption rate of GSH reached 57.8 % in the dark. When in light, the consumption percentage of GSH by PB increased slightly to 33.5 %. Comparatively, the loss of GSH of MoS_2 and MoS_2@PB can reach up to 73.2 % and 90.6 %, respectively. The GSH loss caused by the MoS_2@PB was higher than that by the MoS_2 under the same conditions. Apart from local hyperthermia and ROS yields, the rapid release of iron ions at high temperature can also induce reduction of GSH. The corresponding color change image after GSH processing was shown in Fig. 7b. The color of MoS_2@PB faded almost completely under light, suggesting that GSH oxidation was the most severe, which corresponds well to the results shown in Fig. 7a. Furthermore, the existence of iron ions released from MoS_2@PB was monitored by a inductively coupled plasma atomic emission spectrometry (ICP-AES) in Fig. 7c. The released Fe^{3+} can oxidize the GSH in the bacteria and will be reduced to ferrous ions. The generated ferrous ions will further react with hydrogen peroxide in the bacteria to generate ·OH [35].

What is more, the bacterial membrane permeability was assessed by

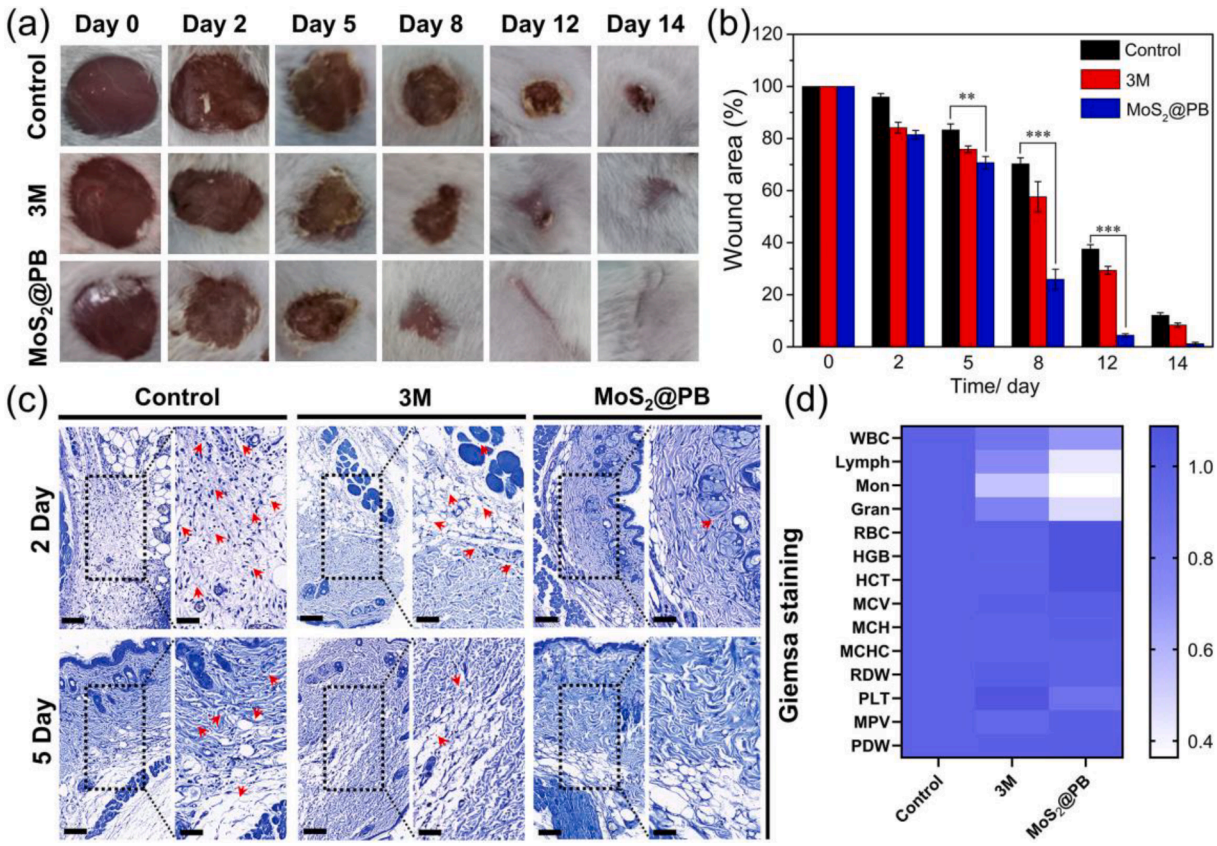

Fig. 10. (a) In vivo antibacterial experiments and wound healing. (b) The process of wound healing (n = 3, $*p < 0.05$, $**p < 0.01$, $***p < 0.001$). (c) The Giemsa staining of wound tissue on days 2 and 5. The scale bars of the lower and higher magnification images are 50 μm and 100 μm respectively. (d) Blood routine parameters tested after 8 days of control, 3 M, and MoS_2@PB groups treatment.

ONPG hydrolysis assay to further study the antibacterial mechanism [45,26]. Fig. 7d showed the $OD_{420\ nm}$ value of the samples before and after illumination. The higher value of $OD_{420\ nm}$ indicated the more serious membrane permeability. Under dark conditions, the PB, MoS_2, and MoS_2@PB groups showed a negligible change at the $OD_{420\ nm}$ value compared with the control group, suggesting unchanged bacterial membrane permeability. By contrast, the membrane permeability of the samples improved significantly under light conditions and the MoS_2@PB group exhibited highest value of $OD_{420\ nm}$, which suggested that the synergy of moderate ROS and hyperthermia efficiently increased the membrane permeation of bacteria, thereby the iron ions can more easily penetrate bacterial membrane [63,37]. These results indicated that MoS_2@PB could rapidly kill bacteria under light irradiation due to local hyperthermia, abundant ROS and the released iron ions.

Herein, a possible bacteria-killing mechanism was schematically illustrated in Fig. 8. When the MoS_2@PB irradiated with 660 nm laser irradiation, bacteria in the surrounding the environment were attacked by ROS generated from MoS_2@PB, causing initial oxidative lesions to the bacterial membranes and making the bacteria to be more sensitive to heat [64]. Meanwhile, the elevated temperature produced by the MoS_2@PB under light increased the permeability of bacterial membrane, thus making it easier for iron ions to penetrate the bacterial cell wall and realize the Fenton reaction [35]. Subsequently, the disturbed bacteria continued to be damaged, resulting in bacterial membrane brake and protein leakage. In addition, the MoS_2@PB produced the hyperthermia, more ROS, and prereleased small amount iron ions, which could accelerate the oxidation of GSH to GSSG. Consequently, the intrinsic balance of the bacteria's protective environment was destroyed, which eventually led to bacterial death. In summary, the synergistic action of hyperthermia and ROS make MoS_2@PB nanocomposites possess excellent antibacterial performance.

3.5. *In vitro biocompatibility evaluation*

The cytocompatibility of samples was studied by a 3-(4,5-dimethylthiazol-2-yl)-2,5-diphenyltetrazolium bromide (MTT) method. In Fig. 9a, after 1 day' culture, the MoS_2 group exhibited higher cell viability (119.87 %) than PB (67.34 %) and MoS_2@PB (83.02 %) groups compared with the control group, which attributed to the excellent biocompatibility of MoS_2. This is because the lamellar structure of MoS_2 with a rough surface is beneficial for cellular adhesion and growth [65]. The PB group exhibited slight cytotoxicity due to the excess of released iron ions. However, after 3 and 7 days of culture, with the increase of cultivation time, the cell viability of PB, MoS_2, and MoS_2@PB was over 80 % and 90 %, respectively. The above results indicated the great cytocompatibility of PB, MoS_2, and MoS_2@PB. Also, the cell fluorescent staining was conducted to further investigate cytotoxicity of the samples (Fig. 9b). After 1 day' culture, compared with the PB group, the NIH-3 T3 cells in MoS_2 and MoS_2@PB groups showed more filopodia extensions around, suggesting that the introduction of MoS_2 facilitated fibroblasts to migration and proliferation. It has been reported that this may possibly be due to the high specific surface area of the nanosheet structure of MoS_2, which can promote cell growth and anchoring of filopodia [66,67,32]. Besides that, the cell density of MoS_2@PB increased significantly because of the good biocompatibility of MoS_2. This outcome was in accordance with MTT assay and could further demonstrate that MoS_2@PB had the great cytocompatibility.

In addition, hemolysis tests were used to evaluate the hemolytic activity of materials. Fig. 9c showed that the hemolysis rate of PB, MoS_2, and MoS_2@PB were below internationally recognized standard (5 %), indicating good blood compatibility of materials [68].

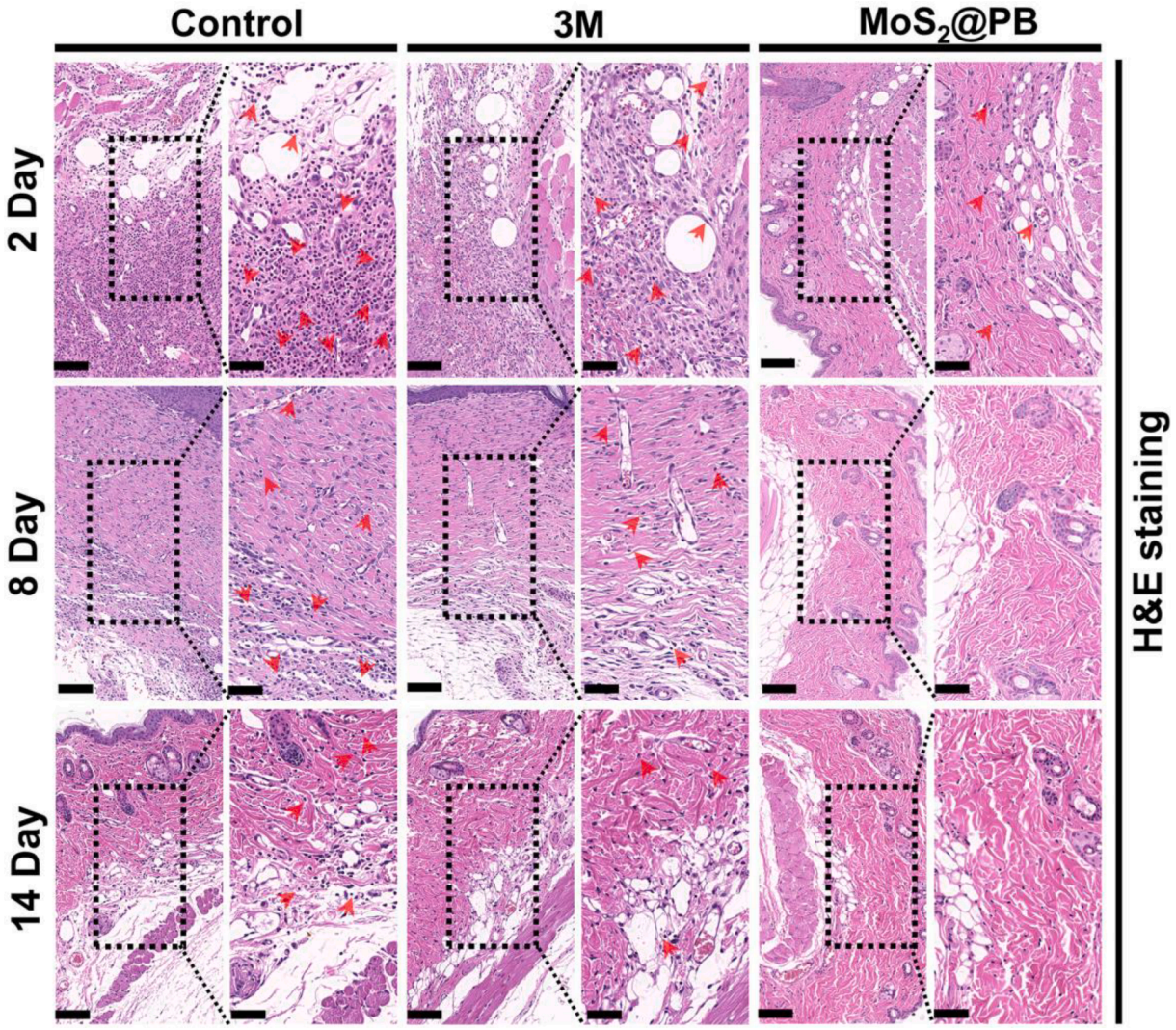

Fig. 11. The H&E staining of wound tissue in all groups on days 2, 8, and 14. Scale bars: 50 μm (high resolution) and 100 μm (low resolution).

3.6. In vivo antibacterial test and wound healing

Animal models were conducted to assess the antimicrobial effect of the samples in wound infection and the effect on wound healing. Fig. 10a evaluated the wound healing process of different samples (control group, 3 M group, MoS_2@PB group). The control and 3 M dressing groups exhibited severe bacterial infection after day 2 of treatment, while the experimental group had fewer bacterial infections, which was in accordance with the *in vitro* antibacterial activity (Fig. 6). After 5, 8, 12, and 14 days of treatment, in comparison with the control and the 3 M groups, the experimental group had the best wound healing rate, and the wound healed completely after 14 days. To clearly observe the speed of wound healing, the quantified changes in wound area over time were shown in Fig. 10b, confirming that the wounds treated with MoS_2@PB healed the fastest. The experimental results showed that MoS_2@PB expressed certain antibacterial and anti-inflammatory effects during the treatment process.

To further investigate wound inflammation, Giemsa and H&E staining were used to examine the recovery of differently treated wounds [63]. The amount of bacteria adhering to the wound on days 2 and 5 was observed by Giemsa staining in Fig. 10c. After 2 days, a large number of bacteria appeared in the control and 3 M groups (indicated by red arrows), while the number of bacteria appeared in MoS_2@PB was less. After 5 days, there were still obvious bacterial residues in the control group. On the contrary, the bacterial number in the MoS_2@PB group was significantly reduced. This suggested that the synergistic antibacterial effect achieves a rapid sterilization and hinders bacterial infection in the body. In addition, Fig. 11 showed histological images of H&E staining after 2, 8, and 14 days. After 14 days, inflammatory cells were still present in the control and 3 M groups, while the MoS_2@PB group had almost no inflammatory cells and most cells were normal. The above experimental results indicated that MoS_2@PB has good antibacterial properties and wound healing ability.

In addition, whole blood of mice in all treatment groups was collected on day 8 for routine blood analysis. As shown in Fig. 10d, the number of white blood cells, lymphocytes, and neutrophils in the control and 3 M groups in the blood routine were obviously higher than that in the material group, suggesting that the MoS_2@PB group had the least amounts of inflammatory cells and the least inflammation in the mice. Furthermore, the hemoglobin concentration (HGB), the number of red blood cells (RBC) and the hematocrit (HCT) in the MoS_2@PB group were remarkably greater than that of the control and 3 M groups. This is because the hemoglobin molecular formula consists of four molecules of hemoglobin and four molecules of heme, and the slow release of Fe^{2+} contributes to the production of hemoglobin. Besides, there were no significant differences in other blood routine parameters between the different groups. Routine blood data again demonstrated that MoS_2@PB possessed the best therapeutic effect on bacterial infection *in vivo*.

As shown in Fig. S18, after 14 days of treatment, the H&E staining of the main organs (heart, liver, spleen, lung and kidney) of mice in different groups did not exhibit any abnormal damage, indicating that MoS_2@PB had no obvious damage to the treated tissue and can be employed for long-term treatment of wounds.

4. Conclusion

In summary, bio-functionalized MoS_2@PB composite was successfully prepared and first explored for rapid sterilization. The photodynamic mechanism at the heterointerface was verified by theoretical calculations based on energy evolution pathways and charge transfer. In addition to the rapid transport of photogenerated charges and the suppresses of photocarriers recombination between PB and MoS_2, the photocatalytic activity of MoS_2@PB were significantly enhanced due to the lower O_2 adsorption energy and higher charge transfer amount toward the adsorptive O_2. Furthermore, the photothermal effect of the system was improved due to the introduction of PB. The MoS_2@PB had good chemical stability and repeated photothermal stability. When exposed to 660 nm visible light irradiation, MoS_2@PB exhibited an antimicrobial efficiency of 99.73 % and 99.58 % against *S. aureus* and *E. coli* severally within 20 min. Also, the oxidation of GSH to GSSG was accelerated through the synergy action of generated ROS, hyperthermia, and the released iron ions. Owing to the low toxicity of the material, the MoS_2@PB had good biocompatibility. Synchronously, from the treatment results of the wound infection model, MoS_2@PB can quickly kill bacteria in the wound and inhibit inflammation to promote wound healing. The blood routine results also showed that the experimental group had a higher hemoglobin level than other groups because of the slow release of iron ions. We believe that this study will bring new perspectives for the development of safe, rapid, controllable, and highly effective therapeutic strategies.

5. Data availability

Data will be made available on request.

Declaration of Competing Interest

The authors declare that they have no known competing financial interests or personal relationships that could have appeared to influence the work reported in this paper.

Acknowledgements

This work is jointly supported by the National Natural Science Foundation of China (Nos. 51871162, 52173251, 82002303), the China National Funds for Distinguished Young Scholars (No. 51925104), Scientific Research Foundation of Peking University Shenzhen Hospital (KYQD2021064), and NSFC-Guangdong Province Joint Program (Key program no. U21A2084). The Central Guidance on Local Science and Technology Development Fund of Hebei Province (226Z1303G). Guangdong Basic and Applied Basic Research Foundation (2021A1515220093, 2022A1515011536).

Appendix A. Supplementary data

Supplementary data to this article can be found online at https://doi.org/10.1016/j.cej.2022.139127.

References

[1] S.H. Hodgson, K. Mansatta, G. Mallett, V. Harris, K.R.W. Emary, A.J. Pollard, What defines an efficacious COVID-19 vaccine? A review of the challenges assessing the clinical efficacy of vaccines against SARS-CoV-2, Lancet, Infect. Dis. 21 (2021) e26–e35, https://doi.org/10.1016/S1473-3099(20)30773-8.

[2] World Health Organization, WHO Coronavirus Disease (COVID-19) Dashboard, March 14, 2022. https://covid19.who.int.

[3] F. Zhou, T. Yu, R.H. Du, G.H. Fan, Y. Liu, Z.B. Liu, J. Xiang, Y.M. Wang, B. Song, X. Y. Gu, L.L. Guan, Y. Wei, H. Li, X.D. Wu, J.Y. Xu, S.J. Tu, Y. Zhang, H. Chen, B. Cao, Clinical course and risk factors for mortality of adult inpatients with COVID-19 in Wuhan, China: a retrospective cohort study, The lancet. 395 (2020) 1054–1062, https://doi.org/10.1016/S0140-6736(20)30566-3.

[4] C.J. Leaver, J. Edelman, Antibiotics as a means of control of bacterial contamination of storage tissue disks, Nature 207 (1965) 1000–1001, https://doi.org/10.1038/2071000a0.

[5] L.S.J. Roope, R.D. Smith, K.B. Pouwels, J. Buchanan, L. Abel, P. Eibich, C.C. Butler, P.S. Tan, A.S. Walker, J.V. Robotham, S. Wordsworth, The challenge of antimicrobial resistance: what economics can contribute, Science 364 (2019) eaau4679, https://doi.org/10.1126/science.aau4679.

[6] E. Bakkeren, M. Diard, W.-D. Hardt, Evolutionary causes and consequences of bacterial antibiotic persistence, Nat. Rev. Microbiol. 18 (2020) 479–490, https://doi.org/10.1038/s41579-020-0378-z.

[7] P. Grenni, V. Ancona, A.B. Caracciolo, Ecological effects of antibiotics on natural ecosystems: A review, Microchem. J. 136 (2018) 25–39, https://doi.org/10.1016/j.microc.2017.02.006.

[8] L. L. Zhang, J. N. Sha, R. R. Chen, Q. Liu, J. Y. Liu, J. Yu, H. S. Zhang, C. G. Lin, W. Zhou, J. W, Surface plasma Ag-decorated Bi_5O_7I microspheres uniformly distributed on a zwitterionic fluorinated polymer with superfunctional antifouling property, Appl. Catal. B Environ. 271 (2020) 118920. https://doi.org/10.1016/j.apcatb.2020.118920.

[9] Y.B. Jin, J.T. Long, X. Ma, T.H. Zhou, Z.Z. Zhang, H.X. Lin, J.L. Long, X.X. Wang, Synthesis of caged iodine-modified ZnO nanomaterials and study on their visible light photocatalytic antibacterial properties, Appl. Catal. B Environ. 256 (2019), 117873, https://doi.org/10.1016/j.apcatb.2019.117873.

[10] M. Chauhan, B. Sharma, R. Kumar, G.R. Chaudhary, A.A. Hassan, S. Kumar, Green synthesis of CuO nanomaterials and their proficient use for organic waste removal and antimicrobial application, Environ. Res. 168 (2019) 85–95, https://doi.org/10.1016/j.envres.2018.09.024.

[11] F.Y. Song, Y. Kong, C.Y. Shao, Y. Cheng, J. Lu, Y.H. Tao, J. Du, H.S. Wang, Chitosan-based multifunctional flexible hemostatic bio-hydrogel, Acta. Biomater. 136 (2021) 170–183, https://doi.org/10.1016/j.actbio.2021.09.056.

[12] Q. Gao, M. Yu, Y.J. Su, M.H. Xie, X. Zhao, P. Li, P.X. Ma, Rationally designed dual functional block copolymers for bottlebrush-like coatings: In vitro and in vivo antimicrobial, antibiofilm, and antifouling properties, Acta. Biomater. 51 (2017) 112–124, https://doi.org/10.1016/j.actbio.2017.01.061.

[13] C.M. Jones, E.M.V. Hoek, A review of the antibacterial effects of silver nanomaterials and potential implications for human health and the environment, J. Nanopart. Res. 12 (2010) 1531–1551, https://doi.org/10.1007/s11051-010-9900-y.

[14] A. Besinis, T.D. Peralta, C.J. Tredwin, R.D. Handy, Review of nanomaterials in dentistry: interactions with the oral microenvironment, clinical applications, hazards, and benefits, ACS Nano. 9 (2015) 2255–2289, https://doi.org/10.1021/nn505015e.

[15] C.G. Allué, A. Tlili, K. Schirmer, M.O. Gessner, R. Behra, Long-term exposure to silver nanoparticles affects periphyton community structure and function, Environ. Sci.: Nano. 5 (2018) 1397–1407, https://doi.org/10.1039/c8en00132d.

[16] A. Panáček, L. Kvítek, M. Smékalová, R. Večeřová, M. Kolář, M. Röderová, F. Dyčka, M. Šebela, R. Prucek, O. Tomanec, R. Zbořil, Bacterial resistance to silver nanoparticles and how to overcome it, Nat. Nanotechnol. 13 (2018) 65–71, https://doi.org/10.1038/s41565-017-0013-y.

[17] J.N. Fu, Y. Li, Y. Zhang, Y.Q. Liang, Y.F. Zheng, Z.Y. Li, S.L. Zhu, C.Y. Li, Z.D. Cui, S.L. Wu, An Engineered Pseudo-Macrophage for Rapid Treatment of Bacteria-Infected Osteomyelitis via Microwave-Excited Anti-Infection and Immunoregulation, Adv. Mater. 33 (2021) 2102926, https://doi.org/10.1002/adma.202102926.

[18] M.Q. Wu, Z.Y. Zhang, Z.R. Liu, J.M. Zhang, Y.L. Zhang, Y.M. Ding, T. Huang, D. L. Xiang, Z. Wang, Y.J. Dai, X.Y. Wan, S.B. Wang, H.L. Qian, Q.J. Sun, L.L. Li, Piezoelectric nanocomposites for sonodynamic bacterial elimination and wound healing, NANO Today. 37 (2021), 101104, https://doi.org/10.1016/j.nantod.2021.101104.

[19] D.L. Han, M.X. Ma, Y.J. Han, Z.D. Cui, Y.Q. Liang, X.M. Liu, Z.Y. Li, S.L. Zhu, S. L. Wu, Eco-friendly hybrids of carbon quantum dots modified MoS_2 for rapid microbial inactivation by strengthened photocatalysis, ACS Sustain. Chem. Eng. 8 (2020) 534–542, https://doi.org/10.1021/acssuschemeng.9b06045.

[20] W.B.F. Chen, J. Chen, L. Li, X.Y. Wang, Q.F. Wei, R.A. Ghiladi, Q.Q. Wang, Wool/Acrylic Blended Fabrics as Next-Generation Photodynamic Antimicrobial Materials, ACS Appl. Mater. Interfaces. 11 (2019) 29557–29568, https://doi.org/10.1021/acsami.9b09625.

[21] C.Y. Yang, Y.D. Chen, W. Guo, Y. Gao, C.Q. Song, Q. Zhang, N.N. Zheng, X.J. Han, C.S. Guo, Bismuth ferrite-based nanoplatform design: an ablation mechanism study of solid tumor and NIR-triggered photothermal/photodynamic combination cancer therapy, Adv. Funct. Mater. 28 (2018) 1706827, https://doi.org/10.1002/adfm.201706827.

[22] Y. Luo, X.M. Liu, L. Tan, Z.Y. Li, K.W.K. Yeung, Y.F. Zheng, Z.D. Cui, Y.Q. Liang, S. L. Zhu, C.Y. Li, X.B. Wang, S.L. Wu, Enhanced photocatalytic and photothermal properties of ecofriendly metal-organic framework heterojunction for rapid sterilization, Chem. Eng. J. 405 (2021), 126730, https://doi.org/10.1016/j.cej.2020.126730.

[23] Q. Wu, L. Tan, X.M. Liu, Z.Y. Li, Y. Zhang, Y.F. Zheng, Y.Q. Liang, Z.D. Cui, S. L. Zhu, S.L. Wu, The enhanced near-infrared photocatalytic and photothermal

effects of MXene-based heterojunction for rapid bacteria-killing, Appl. Catal. B Environ. 297 (2021), 120500, https://doi.org/10.1016/j.apcatb.2021.120500.
[24] P.P. Liang, X.Y. Huang, Y. Wang, D.P. Chen, C.J. Ou, Q. Zhang, J.J. Shao, W. Huang, X.C. Dong, Tumor-microenvironment-responsive nanoconjugate for synergistic anti-vascular activity and phototherapy, ACS Nano. 12 (2018) 11446–11457, https://doi.org/10.1021/acsnano.8b06478.
[25] X.C. Li, 2-Phenyl-4, 4, 5, 5-tetramethylimidazoline-1-oxyl 3-oxide (PTIO•) radical scavenging: a new and simple antioxidant assay in vitro, J. Agric. Food Chem. 65 (2017) 6288–6297, https://doi.org/10.1021/acs.jafc.7b02247.
[26] C.Y. Mao, Y.M. Xiang, X.M. Liu, Y.F. Zheng, K.W.K. Yeung, Z.D. Cui, X.J. Yang, Z. Y. Li, Y.Q. Liang, S.L. Zhu, S.L. Wu, Local photothermal/photodynamic synergistic therapy by disrupting bacterial membrane to accelerate reactive oxygen species permeation and protein leakage, ACS Appl. Mater. Interfaces. 11 (2019) 17902–17914, https://doi.org/10.1021/acsami.9b05787.
[27] Y.T. Zhao, S.C. Jiang, X. Zhao, J.G. Chen, Y.J. Yang, Effect of interband polarization on a solid's high-order-harmonic generation just belowthe band gap, Opt. Lett. 45 (2020) 2874–2877, https://doi.org/10.1364/OL.389787.
[28] K. Wu, X.X. Li, W.Y. Wang, Y.P. Huang, Q.K. Jiang, W.S. Li, Y.Q. Chen, Y.Q. Yang, C.Z. Li, Creating Edge Sites within the Basal Plane of a MoS_2 Catalyst for Substantially Enhanced Hydrodeoxygenation Activity, ACS Catal. 12 (2022) 8–17, https://doi.org/10.1021/acscatal.1c03669.
[29] Y.C. Lin, D.O. Dumcenco, Y.S. Huang, K. Suenaga, Atomic mechanism of the semiconducting-to-metallic phase transition in single-layered MoS_2, Nat. Nanotechnol. 9 (2014) 391–396, https://doi.org/10.1038/NNANO.2014.64.
[30] V. Yadav, S. Roy, P. Singh, Z. Khan, A. Jaiswal, 2D MoS_2-based nanomaterials for therapeutic, bioimaging, and biosensing applications, Small. 15 (2019) 1803706, https://doi.org/10.1002/smll.201803706.
[31] L. Shi, W. Ding, S.P. Yang, Z. He, S.Q. Liu, Rationally designed MoS_2/protonated g-C_3N_4 nanosheet composites as photocatalysts with an excellent synergistic effect toward photocatalytic degradation of organic pollutants, J. Hazard. Mater. 347 (2018) 431–441, https://doi.org/10.1016/j.jhazmat.2018.01.010.
[32] C.F. Wang, Y. Luo, X.M. Liu, Z.D. Cui, Y.F. Zheng, Y.Q. Liang, Z.Y. Li, S.L. Zhu, J. Lei, X.B. Feng, S.L. Wu, The enhanced photocatalytic sterilization of MOF-Based nanohybrid for rapid and portable therapy of bacteria-infected open wounds, Bioact. Mater. 13 (2022) 200–211, https://doi.org/10.1016/j.bioactmat.2021.10.033.
[33] H.L. Shi, C.H. Li, L. Wang, W.T. Wang, X.C. Meng, Selective reduction of nitrate into N_2 by novel Z-scheme NH_2-MIL-101 (Fe)/$BiVO_4$ heterojunction with enhanced photocatalytic activity, J. Hazard. Mater. 424 (2022), 127711, https://doi.org/10.1016/j.jhazmat.2021.127711.
[34] D.D. Wang, J.J. Zhou, R.H. Chen, R.H. Shi, G.Z. Zhao, G.L. Xia, R. Li, Z.B. Liu, J. Tian, H.J. Wang, Z. Guo, H.B. Wang, Q.W. Chen, Controllable synthesis of dual-MOFs nanostructures for pH-responsive artemisinin delivery, magnetic resonance and optical dual-model imaging-guided chemo/photothermal combinational cancer therapy, Biomaterials 100 (2016) 27–40, https://doi.org/10.1016/j.biomaterials.2016.05.027.
[35] S.B. Wei, Y.Q. Qiao, Z.C. Wu, X.M. Liu, Y. Li, Z.D. Cui, C.Y. Li, Y.F. Zheng, Y. Q. Liang, Z.Y. Li, S.L. Zhu, H.R. Wang, X.B. Wang, R.C. Che, S.L. Wu, Na^+ inserted metal-organic framework for rapid therapy of bacteria-infected osteomyelitis through microwave strengthened Fenton reaction and thermal effects, NANO Today. 37 (2021), 101090, https://doi.org/10.1016/j.nantod.2021.101090.
[36] R. Long, K.K. Mao, X.D. Ye, W.S. Yan, Y.B. Huang, J.Y. Wang, Y. Fu, X.S. Wang, X. J. Wu, Y. Xie, Y.J. Xiong, Surface facet of palladium nanocrystals: a key parameter to the activation of molecular oxygen for organic catalysis and cancer treatment, J. Am. Chem. Soc. 135 (2013) 3200–3207, https://doi.org/10.1021/ja311739v.
[37] J. Li, S. Song, J.S. Meng, L. Tan, X.M. Liu, Y.F. Zheng, Z.Y. Li, K.W.K. Yeung, Z. D. Cui, Y.Q. Liang, S.L. Zhu, X.C. Zhang, S.L. Wu, 2D MOF periodontitis photodynamic ion therapy, J. Am. Chem. Soc. 143 (2021) 15427–15439, https://doi.org/10.1021/jacs.1c07875.
[38] P. Zhu, Y. Chen, J.L. Shi, Nanoenzyme-augmented cancer sonodynamic therapy by catalytic tumor oxygenation, ACS Nano. 12 (2018) 3780–3795, https://doi.org/10.1021/acsnano.8b00999.
[39] X.B. Feng, J. Lei, L. Ma, Q.L. Ouyang, Y.X. Zeng, H. Liang, C.C. Lei, G.C. Li, L. Tan, X.M. Liu, C. Yang, Ultrasonic Interfacial Engineering of MoS_2-Modified Zn Single-Atom Catalysts for Efficient Osteomyelitis Sonodynamic Ion Therapy, Small. 18 (2022) 2105775, https://doi.org/10.1002/smll.202105775.
[40] X.B. Feng, L. Ma, J. Lei, Q.L. Ouyang, Y.X. Zeng, Y. Luo, X.G. Zhang, Y. Song, G. C. Li, L. Tan, X.M. Liu, C. Yang, Piezo-Augmented Sonosensitizer with Strong Ultrasound-Propelling Ability for Efficient Treatment of Osteomyelitis, ACS Nano. 16 (2022) 2546–2557, https://doi.org/10.1021/acsnano.1c09189.
[41] J.F. Li, Z.Y. Li, X.M. Liu, C.Y. Li, Y.F. Zheng, K.W.K. Yeung, Z.D. Cui, Y.Q. Liang, S. L. Zhu, W.B. Hu, Y.J. Qi, T.J. Zhang, X.B. Wang, S.L. Wu, Interfacial engineering of Bi_2S_3/Ti_3C_2Tx MXene based on work function for rapid photo-excited bacteria-killing, Nat. Commun. 12 (2021) 1224, https://doi.org/10.1038/s41467-021-21435-6.
[42] H.Y. Shen, C.Y. Jiang, W. Li, Q.F. Wei, R.A. Ghiladi, Q.Q. Wang, Synergistic Photodynamic and Photothermal Antibacterial Activity of In Situ Grown Bacterial Cellulose/MoS_2–Chitosan Nanocomposite Materials with Visible Light Illumination, ACS Appl. Mater. Interfaces. 13 (2021) 31193–31205, https://doi.org/10.1021/acsami.1c08178.
[43] Z.Z. Feng, X.M. Liu, L. Tan, Z.D. Cui, X.J. Yang, Z.Y. Li, Y.F. Zheng, K.W.K. Yeung, S.L. Wu, Electrophoretic deposited stable chitosan@MoS_2 coating with rapid in situ bacteria-killing ability under dual-light irradiation, Small. 14 (2018) 1704347, https://doi.org/10.1002/smll.201704347.
[44] T.I. Kim, B. Kwon, J.H. Yoon, I.J. Park, G.S. Bang, Y.K. Park, Y.S. Seo, S.Y. Choi, Antibacterial activities of graphene oxide–molybdenum disulfide nanocomposite films, ACS Appl. Mater. Interfaces. 9 (2017) 7908–7917, https://doi.org/10.1021/acsami.6b12464.
[45] W. Hong, Y.N. Zhao, Y.R. Guo, C.C. Huang, P. Qiu, J. Zhu, C. Chu, H. Shi, M.C. Liu, PEGylated self-assembled nano-bacitracin A: probing the antibacterial mechanism and real-time tracing of target delivery in vivo, ACS Appl. Mater. Interfaces. 10 (2018) 10688–10705, https://doi.org/10.1021/acsami.8b00135.
[46] H.P. Lee, G. Lokhande, K.A. Singh, M.K. Jaiswal, S. Rajput, A.K. Gaharwar, Light-Triggered In Situ Gelation of Hydrogels using 2D Molybdenum Disulfide (MoS_2) Nanoassemblies as Crosslink Epicenter, Adv. Mater. 33 (2021) 2101238, https://doi.org/10.1002/adma.202101238.
[47] S.A. Shah, L. Xu, R. Sayyar, T. Bian, Z.Y. Liu, A.H. Yuan, X.P. Shen, I. Khan, A. A. Tahir, H. Ullah, Growth of MoS_2 nanosheets on M@N-doped carbon particles (M= Co, Fe or CoFe Alloy) as an efficient electrocatalyst toward hydrogen evolution reaction, Chem. Eng. J. 428 (2022), 132126, https://doi.org/10.1016/j.cej.2021.132126.
[48] Y. Zhang, L. Hu, Y.C. Zhang, X.Z. Wang, H.G. Wang, Snowflake-Like Cu_2S/MoS_2/Pt heterostructure with near infrared photothermal-enhanced electrocatalytic and photoelectrocatalytic hydrogen production, Appl. Catal. B Environ. 315 (2022), 121540, https://doi.org/10.1016/j.apcatb.2022.121540.
[49] L.C. Zhang, J. Liang, Y.Y. Wang, T. Mou, Y.T. Lin, L.C. Yue, T.S. Li, Q. Liu, Y.L. Luo, N. Li, B. Tang, Y. Liu, S.Y. Gao, A.A. Alshehri, X.D. Guo, D.W. Ma, X.P. Sun, High-Performance Electrochemical NO Reduction into NH_3 by MoS_2 Nanosheet, Angew. Chem. Int. Ed. 133 (2021) 25467–25472, https://doi.org/10.1002/anie.202110879.
[50] W. Chen, Y.Z. Wu, Y.F. Yue, J. Liu, W.J. Zhang, X.D. Yang, H. Chen, E.B. Bi, I. Ashraful, M. Grätzel, L.Y. Han, Efficient and stable large-area perovskite solar cells with inorganic charge extraction layers, Science 350 (2015) 944–948, https://doi.org/10.1126/science.aad1015.
[51] J.D. Xiao, Q.Q. Shang, Y.J. Xiong, Q. Zhang, Y. Luo, S.H. Yu, H.L. Jiang, Boosting photocatalytic hydrogen production of a metal–organic framework decorated with platinum nanoparticles: The platinum location matters, Angew. Chem. Int. Ed. 55 (2016) 9389–9393, https://doi.org/10.1002/anie.201603990.
[52] S.H. Su, J.L. Wang, E. Vargas, J.H. Wei, R.M. Zaguilán, S.R. Sennoune, M. L. Pantoya, S. Wang, J. Chaudhuri, J.J. Qiu, Porphyrin immobilized nanographene oxide for enhanced and targeted photothermal therapy of brain cancer, ACS Biomater. Sci. Eng. 2 (2016) 1357–1366, https://doi.org/10.1021/acsbiomaterials.6b00290.
[53] F.F. Abdi, L.H. Han, A.H.M. Smets, M. Zeman, B. Dam, R.V.D. Krol, Efficient solar water splitting by enhanced charge separation in a bismuth vanadate-silicon tandem photoelectrode, Nat. Commun. 4 (2013) 2195, https://doi.org/10.1038/ncomms3195.
[54] L.L. Zhang, P. Chen, J.L. Wang, H.F. Li, W.B. Sun, P.F. Yan, Anthracene-decorated TiO_2 thin films with the enhanced photoelectrochemical performance, J. Colloid Interface Sci. 530 (2018) 624–630, https://doi.org/10.1016/j.jcis.2018.07.016.
[55] Y. Li, W. Zhang, J.F. Niu, Y.S. Chen, Mechanism of photogenerated reactive oxygen species and correlation with the antibacterial properties of engineered metal-oxide nanoparticles, ACS Nano. 6 (2012) 5164–5173, https://doi.org/10.1021/nn300934k.
[56] A. Agresti, A. Pazniak, S. Pescetelli, A. Di Vito, D. Rossi, A. Pecchia, M. Auf der Maur, A. Liedl, R. Larciprete, D.V. Kuznetsov, D. Saranin, A., Di Carlo, Titanium-carbide MXenes for work function and interface engineering in perovskite solar cells, Nat. mater. 18 (2019) 1228–1234, https://doi.org/10.1038/s41563-019-0478-1.
[57] Y.M. Zhang, J.H. Zhao, H. Wang, B. Xiao, W. Zhang, X.B. Zhao, T.P. Lv, M. Thangamuthu, J. Zhang, Y. Guo, J.N. Ma, L.N. Lin, J.W. Tang, R. Huang, Q. J. Liu, Single-atom Cu anchored catalysts for photocatalytic renewable H_2 production with a quantum efficiency of 56%, Nat. Commun. 13 (2022) 58, https://doi.org/10.1038/s41467-021-27698-3.
[58] Y. Nosaka, A.Y. Nosaka, Generation and detection of reactive oxygen species in photocatalysis, Chem. Rev. 117 (2017) 11302–11336, https://doi.org/10.1021/acs.chemrev.7b00161.
[59] R.R. Wang, X. Zhang, F. Li, D. Cao, M. Pu, D.D. Han, J.J. Yang, X. Xiang, Energy-level dependent H_2O_2 production on metal-free, carbon-content tunable carbon nitride photocatalysts, J. Energy Chem. 27 (2018) 343–350, https://doi.org/10.1016/j.jechem.2017.12.014.
[60] Q.H. Qiu, S.Y. Chen, Y.P. Li, Y.C. Yang, H.N. Zhang, Z.Z. Quan, X.H. Qin, R. W. Wang, J.Y. Yu, Functional nanofibers embedded into textiles for durable antibacterial properties, Chem. Eng. J. 384 (2020), 123241, https://doi.org/10.1016/j.cej.2019.123241.
[61] X.L. Nie, S.L. Wu, F.L. Huang, Q.Q. Wang, Q.F. Wei, Smart Textiles with Self-Disinfection and Photothermochromic Effects, ACS Appl. Mater. Interfaces. 13 (2021) 2245–2255, https://doi.org/10.1021/acsami.0c18474.
[62] W.Y. Yin, J. Yu, F.T. Lv, L. Yan, L.R. Zheng, Z.J. Gu, Y.L. Zhao, Functionalized nano-MoS_2 with peroxidase catalytic and near-infrared photothermal activities for safe and synergetic wound antibacterial applications, ACS Nano. 10 (2016) 11000–11011, https://doi.org/10.1021/acsnano.6b05810.
[63] J. Li, X.M. Liu, L. Tan, Z.D. Cui, X.J. Yang, Y.Q. Liang, Z.Y. Li, S.L. Zhu, Y.F. Zheng, K.W.K. Yeung, X.B. Wang, S.L. Wu, Zinc-doped Prussian blue enhances photothermal clearance of Staphylococcus aureus and promotes tissue repair in infected wounds, Nat. Commun. 10 (2019) 4490, https://doi.org/10.1038/s41467-019-12429-6.
[64] X.Z. Xie, C.Y. Mao, X.M. Liu, Y.Z. Zhang, Z.D. Cui, X.J. Yang, K.W.K. Yeung, H. B. Pan, P.K. Chu, S.L. Wu, Synergistic bacteria killing through photodynamic and physical actions of graphene oxide/Ag/collagen coating, ACS Appl. Mater. Interfaces. 9 (2017) 26417–26428, https://doi.org/10.1021/acsami.7b06702.

[65] M.X. Ma, X.M. Liu, L. Tan, Z.D. Cui, X.J. Yang, Y.Q. Liang, Z.Y. Li, Y.F. Zheng, K.W. K. Yeung, S.L. Wu, Enhancing the antibacterial efficacy of low-dose gentamicin with 5 minute assistance of photothermy at 50 °C, Biomater. Sci. 7 (2019) 1437–1447, https://doi.org/10.1039/C8BM01539B.

[66] M. Zhu, X.M. Liu, L. Tan, Z.D. Cui, Y.Q. Liang, Z.Y. Li, K.W.K. Yeung, S.L. Wu, Photo-responsive chitosan/Ag/MoS_2 for rapid bacteria-killing, J. Hazard. Mater. 383 (2020), 121122, https://doi.org/10.1016/j.jhazmat.2019.121122.

[67] C.F. Wang, J. Li, X.M. Liu, Z.D. Cui, D.F. Chen, Z.Y. Li, Y.Q. Liang, S.L. Zhu, S. L. Wu, The rapid photoresponsive bacteria-killing of Cu-doped MoS_2, Biomater. Sci. 8 (2020) 4216–4224, https://doi.org/10.1039/D0BM00872A.

[68] T. Li, P.L. Wang, W.B. Guo, X.M. Huang, X.H. Tian, G.R. Wu, B. Xu, F.F. Li, C. Yan, X.J. Liang, H.M. Lei, Natural berberine-based Chinese herb medicine assembled nanostructures with modified antibacterial application, ACS Nano. 13 (2019) 6770–6781, https://doi.org/10.1021/acsnano.9b01346.